GEOLOGIJA 69/1, 7-34, Ljubljana 2026

https://doi.org/10.5474/geologija.2026.001

Article

Development of the geoelectrical laboratory of the Geological Survey of Slovenia. Part I: Complex electrical signatures of the Mežica Pb-Zn mine waste material and impacted stream sediments

Razvoj geoelektričnega laboratorija Geološkega zavoda Slovenije. 1 del: Kompleksni električni signali Pb-Zn odlagališč rudarskih odpadkov Mežiškega rudišča in potočnih sedimentov

Edmundo PLACENCIA-GÓMEZ[1]*, Martin GABERŠEK[1], Alexis MAINEULT[2], Matthias BÜCKER[3], Philippe LEROY[4], Mateja GOSAR[1], Andrej NOVAK[1] & Nejc BIZJAK[1]

[1]Geological Survey of Slovenia, Dimičeva ulica 14, SI-1000 Ljubljana, Slovenia;
corresponding author*: edmundo.placencia@geo-zs.si
[2]Laboratoire de Géologie, Ecole Normale Supérieure (ENS) / CNRS UMR8538, PSL Research University, 75005 Paris, France
[3]Kiel University, Institute of Geosciences, 24118 Kiel, Germany
[4]BRGM, French Geological Survey, F-45060 Orleans, France

Prejeto / Received 22. 9. 2025; Sprejeto / Accepted 6. 11. 2025; Objavljeno na spletu / Published online 25. 2. 2026

Key words: induced polarization, chargeability, mine waste, sediments, Mežica, Slovenia
Ključne besede: inducirana polarizacija, mera polarizivnosti, rudarski odpadki, sediment, Mežica, Slovenija

Abstract

Environmental geophysical investigations require controlled laboratory experiments to better understand the relationships between the parameters measured in the field and complex physicochemical processes occurring in the subsurface. In this work, we introduce the Geoelectrical Laboratory (GEL) of the Geological Survey of Slovenia. A typical application of the spectral induced polarization (SIP) method, focussing on the detection of electron-conducting minerals disseminated in geologic material is presented. This is demonstrated by the close relationship between the polarization peak values ($\sigma''p$), and chargeability values associated with the second peak (m_2) of polarization spectra estimated from a double Cole-Cole fit, and the metal content, either by the mass % concentration of the ore mineral or the chemical composition (Pb, Zn and Fe) estimated by XRF measurements. We illustrate this for synthetic mixtures of quartz sand and pure Pb-Zn ore particles from the Mežica mine (Slovenia), the Mežica Pb-Zn mine waste material (K-material) and sediments collected from streams near the waste deposits (S-material). These results evidence promising capabilities of the SIP method for *in-situ* detection of metallic particles, both within the mine waste deposits and sediments in the surrounding areas. However, further SIP investigations are needed in a larger number of material samples along with geochemical, mineralogical, and granulometric data to refine the links of polarization and chargeability to both the mass content of ore and the specific geochemical composition of the materials under investigation, as well as to determine the influence of the natural geological materials that constitute both the host rock of Pb-Zn ore and the surrounding sediments (e.g., carbonates).

Izvleček

Okoljske geofizikalne raziskave je za boljše razumevanje odnosov med parametri, merjenimi na terenu, in kompleksnimi fizikalno-kemičnimi procesi v podpovršju treba dopolniti z laboratorijskimi eksperimenti. V prispevku predstavljamo Geoelektrični laboratorij (GEL) Geološkega zavoda Slovenije. Predstavljena je tipična uporaba spektralne inducirane polarizacije (SIP), ki se osredotoča na zaznavanje elektronsko-prevodnih mineralov, ki so razpršeni v geološkem materialu. To je prikazano s tesno povezavo med vrednostmi polarizacijskih viškov ($\sigma''p$) in vrednostmi mer polarizivnosti, povezanimi z drugim viškom (m_2) polarizacijskega spektra, ocenjenega iz dvojnega Cole-Cole modela, ter vsebnostjo kovin, določeno kot masna koncentracija rudnega minerala ali kot kemična sestava (Pb, Zn in Fe), izmerjena z XRF. Tovrstne odnose prikazujemo za sintetične mešanice kremenovega peska in Pb-Zn rude iz Mežiškega rudnika (Slovenija), za Pb-Zn rudarske odpadke iz Mežiškega rudnika (K-material) in sedimente, vzorčene v potokih v neposredni bližini odlagališč (S-material). Rezultati kažejo obetavno možnost uporabe SIP metode za *in-situ* detekcijo kovinskih delcev, tako znotraj odlagališč rudarskih odpadkov kot v potočnih sedimentih v njihovi okolici. Za izboljšanje povezav med polarizacijo in mero polarizivnosti ter masnim deležem rudnih mineralov in specifično geokemično sestavo preiskovanega materiala, kot tudi za opredelitev vpliva naravnih geoloških materialov (npr. karbonatov), so potrebne nadaljnje SIP, geokemične, mineraloške in granulometrične raziskave večjega števila vzorcev.

In 2024, we started developing the Geoelectrical Laboratory (GEL) of the Geological Survey of Slovenia (GeoZS), with the aim of strengthening applied research across the wide range of research fields addressed by GeoZS. The experiment-based research work at GEL, focuses on the development of electrical geophysical methods, with the ultimate objective of providing a non-invasive supplementary technique capable of adding useful insights for addressing urgent problems at the field scale in the areas of environmental engineering, agriculture, hydrogeology, and natural resource management. During phase I of setting up the GEL, our research is focused on the implementation of the spectral induced polarization (SIP) technique, which is based on the measurement of the complex electrical properties of geological materials.

In recent years, the SIP method has probably had the most significant and relevant development among the geoelectrical methodologies for near-surface geophysical investigations, showing promising capabilities for the study of a wide range of physicochemical (electrochemical) mechanisms associated with complex (bio-)geochemical processes occurring in porous media (soils and rocks) (see e.g., Kessouri et al., 2019; Ehosioke et al., 2020, 2024; Binley & Slater, 2020). The growing interest in the SIP method is due to its unique sensitivity to electrochemical properties of the material under investigation, which can be measured at laboratory scale using a relatively simple measuring device. SIP signatures are sensitive to both *electromigration* of ions in the pore fluid associated with the *conductive* properties of the medium, as well as *charge storage* associated with the *capacitive* properties of the various interfaces between different materials within heterogeneous media. Charge storage in saturated porous media mainly occurs within the electrical double layer (EDL) that forms at the surface of the charged solid phase (e.g., the surface of soil grains, minerals, or living microbial cells) from the counterbalance of ions in the electrolyte filling the pores. In the inner part of the EDL, ions are adsorbed to the solid surface (i.e., the structural mineral lattice).

Under the influence of an external electric field, ($\vec{E}$) these ions are only allowed to move tangentially to the solid surface. This thin layer of "fixed" or bound ions in the solution, which carry the opposite sign forms the so-called Stern layer, where strong polarization occurs (Kessouri et al., 2019). Outside the Stern layer, the ionic cloud in the solution forms a diffusion-controlled concentration gradient (as a response to an external electrical field) of length much greater than the inner Stern layer. This outer part of the EDL is called the diffuse layer, and it extends into the pore fluid. In porous media like soils and rocks, the chemical (mineralogical) composition of the solid phase (geologic materials) and the chemistry of the pore water (mainly salinity and pH) determine the electrochemical characteristics of the EDL, e.g., the surface charge density, and cation exchange capacity (CEC), whereas the textural characteristics (e.g., grain or pore size distributions, specific surface area, and tortuosity) of the medium determine the geometry of the EDL. One important geometrical parameter is the typical length scale of connected EDL-covered pore surfaces over which the accumulation (polarization) of charge carriers takes place during SIP measurements. Both, electrochemical and geometrical parameters control the so-called induced polarization (IP) effect and together define the strength of the IP-effect, i.e., the polarization magnitudes, as well as its frequency dependence. The latter is usually presented in terms of a quasi-continuous spectrum of the complex electrical conductivity (or its inverse, the complex electrical resistivity). The real part of these complex quantities is mostly related to ionic conduction and the (usually much smaller) imaginary part to charge storage in the EDLs. In the imaginary part of the complex conductivity, we often observe a maximum or peak at a characteristic frequency, which can be related to a typical EDL or polarization length scale (e.g., grain or pore size).

Not only mineral surfaces are covered by EDLs. Latter also develop in plant cells within roots or tree trunks as well as at the surface of single bacterial cells or cell aggregates (biofilms), giving rise to high IP magnitudes (Kessouri et al., 2019; Abdel Aal et al., 2004; Prodan et al., 2004; Ntarlagiannis et al., 2005; Ntarlagiannis and Ferguson, 2009; Zhang et al., 2014; Martin and Günther, 2013). Developments based on experimental investigations along with developments in sophisticated mechanistic (physicochemical) and phenomenological models of the IP effect (e.g., in silica grains, electron conducting minerals, and clays) as well as in the instrumentation, have broadened the range of possible applications of the SIP method, which is nowadays used to investigate complex processes in a wide range of different fields of geosciences (Binley & Slater, 2020).

Objectives and research scope

The main objective of the present work is to showcase the capabilities of the spectral induced polarization (SIP) method to detect the presence of

metallic particles (Pb-Zn ore particles) in the Mežica Pb-Zn mine waste material and sediments in the vicinity of disposal areas (waste deposits) that have been impacted (contaminated) by the mine waste. Although we focus on the SIP technique, this study envisages the feasibility of other IP-based geophysical techniques (e.g., time-domain IP) for their implementation *in-situ* for detecting and delimiting (large-scale) lateral and vertical (depth) extents of zones associated with disseminated metallic particles, either in the mine waste deposits or their vicinity. Therefore, the scope of this study not only covers the laboratory-scale characterization of the mine waste and impacted sediments by means of SIP measurements, but also the assessment of the IP method for a large-scale and *in-situ* characterization of both the mine waste deposits and the surrounding sediments to the disposal areas. A large-scale geophysical characterization would also allow to strengthen the *in-situ* geochemical characterization typically carried out at specific (point) locations. More importantly, by integrating both geophysical and geochemical approaches, an improved data basis for the management of mine waste disposal facilities could be achieved and help to reduce environmental risks.

Complex electrical conductivity measurements

The measurement of the complex electrical conductivity (σ^*) or its inverse, the complex electrical resistivity ($\rho^*=1/\sigma^*$), assesses both conductive (or resistive) and capacitive properties of Earth geologic materials (soils and rocks). Conductive (or resistive) electrical properties are associated with the movement of charge carriers, which are dragged by the imposed external (sinusoidal) electric field ($\vec{E}$). This movement is due to an electromigration mechanism carried by ions in an electrolyte solution or electrons in a metallic mineral. Electrolytic conductivity by ions constitutes the main charge-transport mechanism in interconnected pore spaces, fissures, and fractures of geological materials, whereas electrons (and holes) are responsible for the transport of electric charge inside metallic (or semi-conducting) minerals (see Binley & Slater, 2020, and references there in for historical development of DC-resistivity and IP methods). Electrons are also involved in charge transfer processes across the mineral-electrolyte interface, which are enabled by redox reactions at the external part of the crystal lattice of metallic minerals and in bacterial metabolism processes, such as the extracellular electron transfer mechanism (cf., geo-batteries). In contrast, the capacitive electrical properties of geologic materials are associated with charge-storage mechanisms which can be seen as analogous to an electrical capacitor. However, in SIP investigations, the polarization process detected in the SIP frequency range is mainly controlled by diffusion of ions in both the Stern and diffuse layers, i.e., within EDLs covering the surface of soils grains and minerals. Depending on the micro-scale geometry of the solid-electrolyte interfaces, dominant polarization length scales may be related to individual grains or ion-selective zones occurring in narrow pore constrictions (pore throats), which may form complex networks of pores, fissures, or fractures. As mentioned above, charge storage in polarized EDLs along with diffusion-controlled processes are the basis of the IP effect observed in low-frequency (< 1 kHz) SIP signatures.

The induced polarization measurements for assessing the IP effect of materials can be carried out in time or frequency domain. In the frequency-domain or spectral mode (SIP), of interest here, conductive (or resistive) and diffusion-controlled capacitive electrical properties are measured in terms of a frequency-dependent complex electrical conductivity, $\sigma^*(\omega)$, or resistivity, $\rho^*(\omega)$, where ω is the angular frequency, $\omega = 2\pi f$ (in rad/s), and f the frequency in Hertz (1/s). Following Ohm's Law, σ^* is the constant of proportionality between the total current density and the applied electric field. Commonly, the measured complex conductivity is expressed in terms of its real σ' and imaginary σ'' component or in terms of its amplitude (magnitude) $|\sigma^*|$ and phase angle (argument) φ as follows,

$$\sigma^* = |\sigma^*| \exp(i\varphi) = \sigma' + i\sigma'', \quad (1)$$

$$\sigma' = |\sigma^*| \cos(\varphi), \quad (2)$$

$$\sigma'' = |\sigma^*| \sin(\varphi), \quad (3)$$

$$|\sigma^*| = \sqrt{(\sigma')^2 + (\sigma'')^2}, \quad (4)$$

$$\varphi = \tan^{-1}\left(\frac{\sigma''}{\sigma'}\right) \approx \frac{\sigma''}{\sigma'}, \text{ for } \varphi < 0.1 \text{ radians} \quad (5)$$

At low frequencies, for instance, between 1 mHz and 45 kHz, which is the range of frequencies used in laboratory SIP measurements, the influence of the diffusion-controlled charge storage mechanisms is small relative to that of electromigration such that $-\varphi$ can be approximated by the ratio between imaginary and real conductivity

(Equation 5). Furthermore, within the frequency range of SIP investigations, the measured $-\varphi$ is commonly below 100 m radians. The real component of the electrical conductivity σ' (in S/m) in Equation 1 contains all the information relative to the conductive properties of geologic materials, i.e., the information relative to electromigration of ions in the free pore fluid and EDL. The imaginary component σ'' (in S/m) mostly contains information on the capacitive properties of geologic materials, i.e., the diffusion-controlled polarization mechanisms in the EDL, containing information on electrochemical characteristics of geological materials, and the polarization length scales of the EDL (i.e., grain surface, pore throats, porewalls, geo-batteries, etc.). The phase angle φ (in radians), reported here after as positive quantity by taking its negative (i.e.,$-\varphi$), quantifies the phase lag or shift between the injected alternating current and the measured voltage. i is the imaginary number, $i=\sqrt{-1}$.

Polarization of electron conducting minerals (metallic particles)

Over the last decades, numerous theoretical studies of the IP effect of electron conducting minerals accompanied by laboratory-scale SIP measurements have shown the capabilities and unique sensitivity of the SIP method to characterize the presence of metallic particles in porous media (Slater et al., 2005, 2006; Placencia-Gómez et al., 2013, 2015; Gurin et al., 2013, 2015, 2018; Revil et al., 2015a,b; Hupfer et al., 2016; Chuprinko & Titov, 2017; Bücker et al., 2018, 2019; Martin et al., 2022; Martin & Weller, 2023; Maineult et al., 2025b).

Wong (1979) was the first to propose a comprehensive physics-based model of the electrochemical origins of the IP effect of metallic particles, involving a diffuse-layer charging mechanism and the effect of oxidation-reduction reactions that take place on the surface of metallic particles and permit a (faradaic) reaction current, i_0, to cross the solid-electrolyte boundary. As the fundamental model by Wong does not correctly predict the vari-

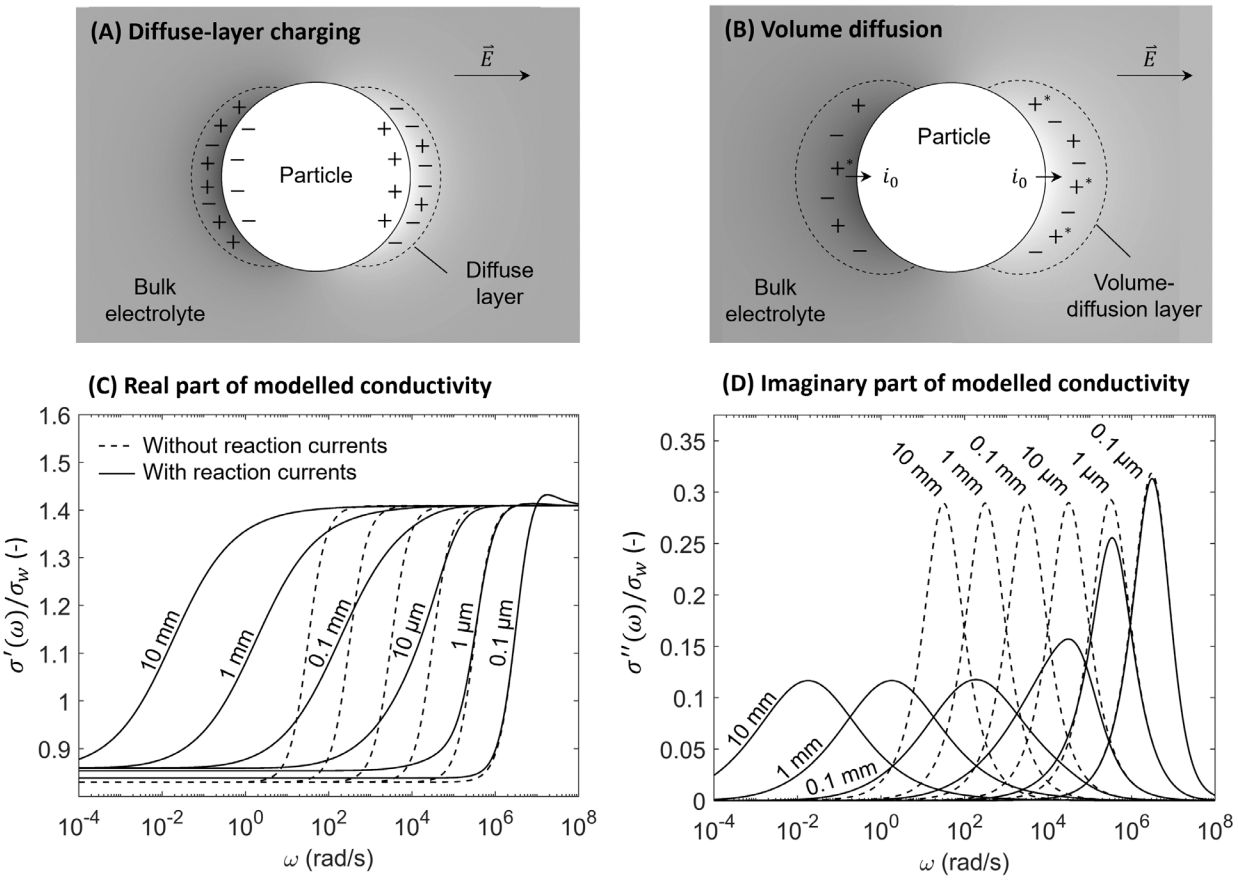

Fig. 1. Conceptualization of the electrochemical polarization of a metallic particle in the absence (A) and presence(B) of redox active ions in the EDL as proposed by Wong (1979) and discussed in detail by Bücker et al. (2018). In the absence of reaction currents, diffuse-layer charging is the dominant polarization mechanism at low frequencies. In the presence of reaction currents, diffuse-layer charging is superimposed by a volume-diffusion mechanism, which leads to the build-up of electrically neutral regions of decreased (left of the particle, if the electrical field points to the right) and increased (right of the particle) salinity. Corresponding real conductivity σ'(C) and imaginary conductivity σ''or polarization (D) spectra (normalized to the fluid conductivity σ_W) for different grain radii between 0.1 µm and 10 mm in the presence (solid lines) and absence (dashed lines) of redox reactions at the solid-electrolyte interface. Figures modified from Bücker et al. (2018).

ation of the characteristic frequency of polarization with the conductivity of the electrolyte, Gurin et al. (2015) propose a semi-empirical model involving a specific polarizability of the metallic particle surface. More recently, Bücker et al. (2018, 2019), revised and extended the model of Wong, providing a more complete conceptual understanding of the IP effect at the surface of metallic particles. They also highlight the important role that the reaction current i_o plays in the IP phenomenon, emphasizing that i_o cannot be neglected as it strongly affects both the maximum imaginary conductivity and the characteristic frequency at which the polarization peak is observed (see Fig. 1).

The complexity of integrating redox reactions into the IP effect of metal particles, primarily lies in the appropriate parameterization of the reaction current i_o through the interface between the mineral surface and the electrolyte and their incorporation into polarization models. This has led to the development of new physical (mechanistic) models, which do consider diffuse-layer charging and possible additional polarization mechanisms within semi-conducting grains (e.g., Revil et al., 2015b; Abdulsamad et al., 2017) but neglect the effect of redox-reactive ions.

In Fig. 1, we illustrate the polarization mechanisms of a spherical metallic particle based on the model by Wong (1979) and visualized by Bücker et al. (2018; 2019) with and without redox reactions. The visualizations show the basic diffuse-layer charging mechanism (panel A) as well as the effect of a reaction current i_o through the solid-electrolyte interface (panel B). The charging of the diffuse layer is analogous to the charging of a capacitor and leads to a strong polarization effect. Reaction currents lead to an imperfect polarization (the so-called "leaky capacitor"), which leads to a shift of the peak frequency, f_p, towards lower frequencies and a broadening of the spectral peak (panel D). The chargeability, which reflects the maximum difference between the real conductivity at low and high frequencies, remains almost unaltered by the effect of reaction currents (panel C). For a more complete discussion of the IP effect of metal-bearing particles, readers are referred to the above-cited literature.

Research strategy for detecting Pb and Zn particles in mine waste material and contaminated sediments

Our research strategy for the detection of metallic particles in the Mežica Pb-Zn mine waste material, referred to as K-material hereafter, and mine waste-contaminated stream sediments, referred to as S-material hereafter, focus on the analysis of polarization spectra (σ''), specifically the polarization peak values (σ''_p) at the corresponding critical frequency, also named peak frequency, (f_p), of SIP signatures, and chargeability (m_2) values, where the latter is estimated from a modelling approach proposed by Maineult et al. (2025a,b) based on a double Cole-Cole fit model:

$$\sigma^*(\omega) = \sigma_0 \left(1 + \frac{m_1}{1-m_1}\left(1 - \frac{1}{1 + (i\omega\tau_1)^{c_1}}\right) + \frac{m_2}{1-m_2}\left(1 - \frac{1}{1 + (i\omega\tau_2)^{c_2}}\right)\right). \quad (6)$$

Here, σ_0 is the low-frequency limit of the sample conductivity (in S/m) almost completely associated with the pore water conductivity (σ_w), $m_{1,2}$ are chargeabilities (in V/V and shown as unitless) related to the charge-storage capacity of the material, $c_{1,2}$ are constants determining the broadness of the relaxation peaks (unitless), and $\tau_{1,2}$ (in s) are the time constants linked to polarization processes. The subscripts 1 and 2 stand for the first and second Cole-Cole relaxation peak, respectively.

To illustrate the detection of Pb and Zn ore particles in the K- and S- material, we have used the grain size fraction <2.0 mm for each type of K- and S- material samples. Additionally, we have characterized the SIP response of the Mežica Pb-Zn particles separately for a grain size fraction <0.2 mm, varying their volume concentration (vol. %) in synthetic mixtures with quartz sand (0.4 – 0.8 mm) as the matrix, hereafter Mž-samples. Recognizing the peak frequency, f_p, where the maximum polarization or peak value, σ''_p, occurs in the SIP response of the Mž-samples, the f_p is used as the reference to associate the corresponding σ''_p values in the SIP response of the K- and S-material samples (< 2.0 mm fraction) with the presence of metallic Pb-Zn particles. Furthermore, we correlate the σ''_p values with the mass concentration (in %) of chemical elements, Pb, Zn, and Fe, estimated by XRF measurements for both the K- and S- material samples, and Mž-samples. Similarly, and as we will see further below the second set of Cole-Cole parameters is associated with the IP-effect of the metallic particles (our target) we correlate the value of chargeability, m_2, with the mass % concentration of Pb-Zn ore particles and with the mass % concentration of chemical elements Pb, Zn, and Fe.

Materials and methods

The Mežica Pb-Zn mine waste deposits

More than 300 years of mining and mineral processing at the Mežica Pb-Zn mine, Northern Slovenia, resulted in the accumulation of large amounts of waste that have been dumped at several steep slopes (deposits) next to the mine. Given these characteristics, the mine waste (K-material) has impacted the surrounding stream sediments (S-material), as a result of the mass movements (spills) and recent extreme rainfall events (floods) in Slovenia. Geochemical analysis in the grain size fraction <0.125 mm of both the K- and S- material samples has shown significant concentrations of potentially toxic elements (PTE), such as Pb, Zn, Cu, Cd, etc. Considering that several streams drain the waste deposits and that they are also tributaries of the Meža river, the sediments along these streams have suffered the impacts of the mine waste (Gosar et al., 2020; 2024; Miler et al., 2022). Mainly the finest particle-size fraction of these riverbed sediments holds large amounts of PTE as the finest particle fraction is easily transported by the natural run-off (water erosion) or by mass movement in suspension after prolongated rainfall events, which in case of flooding and spills poses a risk to the environment and human health.

Sampling and preparation of samples of mine waste-material and stream sediments

Samples of mine waste (K-material) and stream sediment (S-material) from the former Mežica Pb and Zn mine were collected during regular monitoring campaigns for the state authorities in 2024. The K-material was collected at the surface of waste deposits (0–30 cm) and the S-material along the edges of the Meža riverbed down to a depth of about 3 cm. In this way, we collected only the most recent/active stream sediment. Sampling of S-material was performed with a plastic spatula.

In the laboratory, all samples were dried at 35 °C and sieved to four size fractions (2.0–0.63 mm, 0.63 – 0.2 mm, 0.2–0.125 mm, and <0.125 mm) to determine their granulometric composition (Table 1) and to prepare composite samples, i.e., comprising the entire <2.0 mm fraction, for further geochemical and geophysical analyses. As these composite samples integrate all the fractions shown in Table 1, we consider the <2.0 mm grain size fraction samples for SIP measurements are texturally equivalent to the K- and S- material samples collected in the field whose textural features are referred to in Table 1. Additionally, we measured the grain size distribution in all composite samples of <2.0 mm fraction using laser granulometry after being subjected to SIP measurements. The elemental geochemical composition of the size fraction <0.125 mm (no SIP measurements were performed in this fraction) was determined with inductively coupled plasma mass spectrometry (ICP-MS) after *aqua regia* digestion by the Bureau Veritas Commodities (Vancouver, Canada). Whereas the elemental geochemical composition of composite samples (<2.0 mm fraction) used for correlations with SIP measurements was analysed with a handheld XRF analyser. Overall, we analysed three composite samples (<2.0 mm fraction) of mine waste material (K-26.12, K-26.18, K-26.19) and four composite samples (<2.0 mm fraction) of stream sediment (S-26.3, S-26.5, S-26.6, S-26.9), and used the <0.125 mm fraction of the K- and S-material samples in Table 1 as a base for the metallic content analysis (geochemical composition) in the composite samples (<2.0 mm fraction).

Table 1. Granulometric composition of the K- and S- material collected in the field from which each corresponding composite sample was prepared for this study. Composite samples of the entire granulometry (<2.0 mm fraction) were subjected to SIP measurements.

Sample	2.0–0.63 mm coarse sand (vol. %)	0.63–0.20 mm medium sand (vol. %)	0.20–0.125 mm fine sand (vol.%)	<0.125 mm silt/clay (vol.%)
K-26.12	65.70	18.59	4.85	10.86
K-26.18	67.75	18.04	3.82	10.40
K-26.19	55.58	21.93	5.93	16.56
S-26.3	25.32	29.91	13.26	31.51
S-26.5	37.25	45.91	8.90	7.93
S-26.6	9.57	31.80	27.03	31.60
S-26.9	4.71	61.93	22.12	11.24

Synthetic mixtures

Various synthetic mixtures were prepared with pure quartz sand (SiO_2), referred to hereafter as QzS, with particle sizes between 0.4 and 0.8 mm, and Pb-Zn ore collected at the Mežica site, with particle sizes ranging between 0.02 and 0.2 mm, with the purpose of quantifying the IP effect of the Pb-Zn metallic particles. Our premise is that the mine waste material still hosts Pb-Zn particles and that any impact in the surrounding sediments (S-material) will be done by the presence (or contamination) of the Pb-Zn particles. Therefore, the characterization of the IP effect linked to Pb-Zn ore particles alone is needed as a reference.

A total of seven synthetic mixtures (Mž-samples) were prepared with varying content of each component (Table 2). The elemental composition of

Mž-samples was estimated with a handheld XRF analyser before and after the SIP measurements. The grain-size distribution of Mž-samples, as well as of the Pb-Zn ore particles fraction used in the mixtures, was measured using a Fritch Analysette 22 laser granulometer at the Geological Survey of Slovenia. Each Mž-sample was measured three times, and an average particle size was calculated from the three measurements.

Table 2. Composition of synthetic mixtures (Mž-samples). The grain size fraction of QzS (matrix) ranges from 0.4 mm to 0.8 mm and from 0.02 mm to 0.2 mm for the Pb-Zn ore particles in all samples.

Sample	QzS (vol. %)	Pb-Zn Ore (vol. %)	QzS (mass %)	Pb-Zn Ore (mass %)
Mž-1.1	99.5	0.5	98.91	1.09
Mž-1.2	99	1	97.84	2.16
Mž-1.3	98	2	95.72	4.28
Mž-1.4	97	3	93.66	6.34
Mž-1.5	95	5	89.67	10.33
Mž-1.6	90	10	80.44	19.56
Mž-1.7	85	15	72.14	27.86

Experimental procedures

The K- and S- material samples (< 2.0 mm fraction) and the synthetic mixtures (Mž-samples) were first partially moistened with ≈5 ml of the saturation solution separately in plastic bottles, shaken for homogenization, and carefully packed afterwards in acrylic tubes (sample holder) following the procedure of *damp packing* (Lewis & Sjöstrom, 2010, and references therein). This procedure is useful to avoid stratifying layers during packing and preferential flow pathways during saturation. In our case, the moistened and homogenised material in the plastic bottles was added into the sample holder by small amounts or "lifts" of ≈1 cm. At every lift the material was uniformly compacted, lightly breaking up the surface with a scarifier before adding the next lift, repeating the same process until the column was filled, keeping the material immobile during the saturation process. We started the saturation process by capillarity, then by imposing a constant hydraulic head until the pore volume of the sample had been exchanged at least two times by the saturation solution. Finally, we left the columns to rest overnight for chemical equilibration before we started measuring the SIP signature. Since the carbonate rocks that predominate in the study area are rich in Ca^{2+}, the predominant ion in the surface waters in the surroundings of the mine waste deposits is also Ca^{2+}.

Therefore, we used a $CaCl_2$ brine as the saturation fluid at three different salinities determined by their electrical conductivity (EC) values, this latter measured with a regular bench-scale probe and meter in the laboratory. The three salinities yielded ECs of 246 µS/cm, 408 µS/cm, and 680 µS/cm, which are the EC values measured in the field (streams and rivers) with a portable probe and meter at the sampling locations of the S-material. We measured the SIP response in the K- and S- material samples at every EC separately, whereas the SIP response of Mž-samples was only measured at the highest salinity (EC = 680 µS/cm) in order to compare all materials. Therefore, for the assessment of the method to detect the metallic particles we use the SIP signatures measured at EC = 680 µS/cm. The SIP response of the K- and S-material samples to different salinities (giving rise to different pore-water conductivity, σ_w) is useful to evaluate possible effects on the IP signature associated with the presence of metallic particles on the mineral surface, e.g., a shift of f_p towards the higher frequencies with increasing salinity (see e.g., Placencia-Gómez & Slater, 2016, and Hupfer et al., 2016 for the influence of electrolyte conductivity). However, a detailed analysis of the effects associated with changes of salinity is out of the scope of this work and will be analysed separately and in more detail in future investigations.

Setup of laboratory SIP measurements

We used the SIP-COMPACT-S instrument from Radic Research (Germany) to perform the SIP measurements (Fig. A1 in the Appendix). This instrument is mainly designed for laboratory-scale measurements, though field-scale measurements with a limited depth of penetration can be also performed. The SIP-COMPACT-S has four channels, one for the monitoring of the injected current (C1, C2) and three for measuring potential differences (P1-P2, P3-P4, and P4-P5), such that three simultaneous SIP readings can be taken. For the present work, all SIP signals were recorded from 3.8 mHz to 30 kHz, measuring magnitude, $|\sigma^*|$, and phase, $-\varphi$, of the complex conductivity at 24 logarithmically equidistant frequencies (equally spaced on a logarithmic scale). The laboratory measuring device shown in Fig. A1-C, D in the Appendix, consists of a cylindrical acrylic tube (sample holder) mounted on a water reservoir made of PVC at each end of the sample holder. The dimensions of the cylindrical sample holder can vary. We used tubes of 6 cm H (height) × 4.3 cm ID (inner diameter). Depending on whether the geological material is unconsolidated (disturbed) or consolidated

(undisturbed soil or rock samples), and whether saturation is complete or partial, the reservoirs at the ends are filled with the saturation electrolyte (e.g., a brine or water) or agar gel, respectively. In the case of unconsolidated materials (disturbed samples) at fully saturated conditions (this work), we placed a perforated acrylic disc with a filter paper (e.g., 100 μpore) or a nylon mesh at each end of the sample holder to avoid the material being washed out during the saturation process (i.e., while the saturating fluid flows through the sample holder).

Non-polarizable Ag-AgCl potential electrodes (P+, P-) were placed in the water reservoirs at 2 cm distance from both ends of the sample holder (i.e., in contact with the water) and connected to channel P1-P2 of the instrument. By placing the potential electrodes outside the sample holder, we guarantee that the measured potential difference (U^*) between P+ and P- comprises the entire length of the sample, avoiding underestimating in this case the mass % or vol. % of the metal content in the Mž-samples and/or K-and S-material samples. Other alternatives are to place P+ and P- at the ends of the acrylic tubes in contact with the sample to ensure a sensitive volume between P+ and P- that covers the entire sample, using metal rings for example or another type or electrodes, but this needs special instrumentation that we currently do not have available at GEL. Another advantage of placing P+ and P- in the water reservoirs is that we ensure good electrical contact and, most importantly, we avoid touching the material inside the sample holder once it has been packaged. This configuration has been successfully used in other works, for example, Wu et al., 2010, to avoid reactions outside of the sensitive volume between P+ and P- for investigations on induced calcite precipitation with SIP measurements. Furthermore, this configuration is the one used for SIP measurements in consolidated rock core samples of sandstones or carbonates for permeability investigations (e.g., Binley et al., 2005; Peshtani et al., 2024). The current (I^*) flowing through the sample material is imposed from two copper discs placed at the bottom of each water reservoir, referred to as the current electrodes C+ and C-, connected to channels C1 and C2 of the measuring device. The distance between C+ and P+ (and C- and P-) is greater than two times the diameter of the column as recommended by Zimmerman et al. (2008), in this case 11 cm versus 8.6 cm, ensuring that $\vec{E}$ is not distorted in the vicinity of electrodes P+ and P- and thus the potential difference is cleanly measured between the two electrodes. We assume that the potential drop associated with the sensitive volume determined by the 2 × 2 cm distance between the potential electrodes (P+,P-) and the acrylic discs (at each end of the sample holder) is not significant relative to that across the sample material as the latter is usually much more resistive than the saturating fluid filling the remaining volume between sample holder and potential electrodes.

The geometric factor used to convert measured resistance to resistivity is $k_g = \mathrm{A/L}$, where A is the cross section of the material sample and L the length of the acrylic tube (sample) plus the 2 × 2 cm distance between the sample and potential electrodes. The retracted distance of Ag-AgCl electrodes (wires) from the $\vec{E}$ lines (cf. Fig. 1A-D), was also tested to play a role for reducing some distortion observed in the SIP signatures, though these effects were minimal and vanished with increasing the conductivity of the sample and equilibration time.

Calibration measurements

The entire laboratory setup was calibrated by measuring the SIP response of the $CaCl_2$ saturation solution alone at different electrical conductivities (EC), i.e., by varying the salinity (Fig. A2). In the brine alone, only electromigration currents carried by ions moving under the influence of the applied electrical field ($\vec{E}$) occur. Particularly, no polarization effects are expected within the range of frequencies of the SIP measurements and therefore $-\varphi$ (and σ'') is expected to be close to zero. The validation of our home-made measuring device and reliability of SIP measurements consisted of the good matching between the measured magnitude $|\sigma^*|$ and the EC values of each electrolyte (the EC measured with a regular bench-scale probe and conductivity meter in the laboratory) assuming $-\varphi$ or $\sigma'' = 0$. Additionally, the SIP instrument is accompanied with a calibration box (c.f. Fig. A1-B), that consists of a resistor of 120 Ohm, which translates into an expected real-valued conductivity $|\sigma^*|$ (or σ') of 83.33 μS/cm (using a geometrical factor of $k_g = 1$ m) and a vanishing phase, i.e., $-\varphi = 0$ mrad, or imaginary conductivity $\sigma'' = 0$ μS/cm. The relative measurement error of the instrument in terms of $-\varphi$ is 0.2 %.

Furthermore, we used pure quartz sand (QzS), which is known to have no or only a negligible polarization response in the low frequencies, to evaluate the influence of other polarization mechanisms, such as Maxwell-Wagner polarization, or the polarization associated with the stray capacitances resulting from electromagnetic coupling effects caused between potential electrode cables,

or due to the contact impedance of the potential electrodes. All these processes have been observed in measurements on silica sand at frequencies > 100 Hz (Leroy et al., 2008; Leroy & Revil, 2009). All our calibration measurements were done using the nylon mesh and perforated discs, observing no effects in the SIP measured signatures. A good practice is for instance, to check that air bubbles do not get trapped between the samples and the nylon mesh (within the perforations in the acrylic disc) during the packing, as well as to avoid air bubbles on the contact between potential electrodes and the material sample (which is not the case for the used electrode configuration) during the SIP measurements.

The smooth SIP spectra (absence of individual peaks in our SIP data) we recorded during calibration indicated that no air bubbles were formed with either the nylon mesh or the perforated discs. The calibration measurements in $CaCl_2$ alone show a good match between measured magnitudes, $|\sigma*|$ (or σ'), and the EC values of the $CaCl_2$ brines, whereas in the case of saturated QzS the SIP measurement results in much lower $|\sigma^*|$ (or σ') values than the theoretical EC of the saturation electrolyte, as expected due to the presence of non-conducting silica grains. We emphasize in the very small polarizability of QzS in terms of $-\varphi$ and σ'' with similar values as in the case of the brine at frequencies < 10 kHz (cf. Fig. A2). These results, evidence that our measurement device (sample holder and electrode configuration) works properly providing reliable SIP measurements, considering that in saturated QzS the polarization does not exist or is negligible, whereas the magnitudes of σ^* (or σ') in brines alone must be close to the EC value of the brine measured in the laboratory.

Data processing and modelling

The IP effect of disseminated well-sorted metallic particles in porous media commonly shows SIP spectra that are symmetrical with respect to the characteristic peak frequency, f_p, at which $-\varphi$ and σ'' reach their maximum value (peak) and converge to zero or a constant value towards higher/lower frequencies (see e.g., Fig. 1D). However, SIP measurements above 100 Hz can be affected by electromagnetic coupling (EMC), e.g., between cables of the measurement device (e.g., Florsch et al., 2014). The phase shift or imaginary conductivity associated with EMC overlaps with and can significantly affect the targeted low-frequency SIP signatures, particularly in the higher frequencies. Additionally, at frequencies >100 Hz, Maxwell-Wagner (M-W) polarization may also contribute to the measured SIP signatures (Binley & Slater, 2022). Therefore, it is convenient to consider effects occurring at high frequencies by fitting the term $i\omega C$, where C is a capacitance (in F/m), to the high-frequency trend of the spectral response. Once the value of C is determined the term $i\omega C$ can be subtracted to correct the SIP spectrum for effects linked to EMC and/or M-W polarization:

$$\tilde{\sigma}^*(\omega) = \sigma^*(\omega) - i\omega C. \quad (7)$$

Here, $\tilde{\sigma}^*$ is the corrected frequency-dependent complex conductivity, and σ^* the measured frequency-dependent complex conductivity. We used the approach recently proposed by Maineult et al. (2025a) to remove the effects linked to the high-frequency polarization trends from all the SIP signatures. In this approach σ^* is matched with a Debye decomposition facilitating the determination of the term $i\omega C$ and its removal (Equation A1 in Maineult et al., 2025a, for details). Then, the corrected SIP spectra ($\tilde{\sigma}*$) were fitted by a double Cole-Cole relaxation model (Equation 6), using the simulated annealing procedure (Maineult, 2016; Mendieta et al., 2021, 2023). In the Fig. A3 of the Appendix, we show an example of the effectiveness of this approach, which significantly reduces the undesired polarization effects encompassed by the term $i\omega C$ for both K- and S-samples (<2.00 mm fraction).

Results and Discussion

Geochemical composition

XRF measurements in the Mž-samples show higher mass concentrations of Pb than of Zn (%) and low concentrations (<0.1 %) of Fe (Fig. 2-A), whereas in the K- and S-material the elemental geochemical composition varies with respect to the grain size fraction. The highest mass concentration of Pb and Zn (mass %) are observed in the <0.125 mm fraction of K-material samples (Fig. 2-B) measured separately (no SIP measurements were carried out for the grain size fraction <0.125 mm of K- and S-material samples), followed by Fe (Fig. 2-C). In contrast, for the K- and S- material samples of grain size fraction <2.0 mm used for SIP measurements, Fe concentrations were higher than concentrations of Pb and Zn, with significantly greater concentration in the S- than in the K- samples (Fig. 2-C). The average of mass concentrations of Pb and Zn (%) measured in the K- and S-material samples (<2.0 mm fraction) from before and after the SIP measurement were much lower than in the grain size fraction <0.125 mm

of K- and S-material samples (Fig. 2-D). However, among the K-samples (<2.0 mm fraction), only sample K-26.12 shows significantly higher Fe concentration than Pb and Zn.

The granulometric analysis (Fig. 3-A) shows that the Mž-samples have a similar grain-size distribution as the matrix QzS, while Pb-Zn ore particles tend to have a smaller grain size distribution (i.e., between 0.02 mm and 0.2 mm in Fig. 3). Analogously, in the K- and S-material samples, the grain size fraction <0.2 mm might be associated with the presence of metallic particles, such as Pb-Zn particles (Fig. 3-B). As observed in Fig. 3-B, results show the 80 % by volume in the K-material samples is below 0.2 mm size fraction, whereas the S-material samples show up to 70 % by volume of fraction <0.2 mm (S-26.3 and S-26.6), followed by S-26.9 with 50 %, and S-26.5 with 20 % by volume of grain size fraction <0.2 mm, respectively.

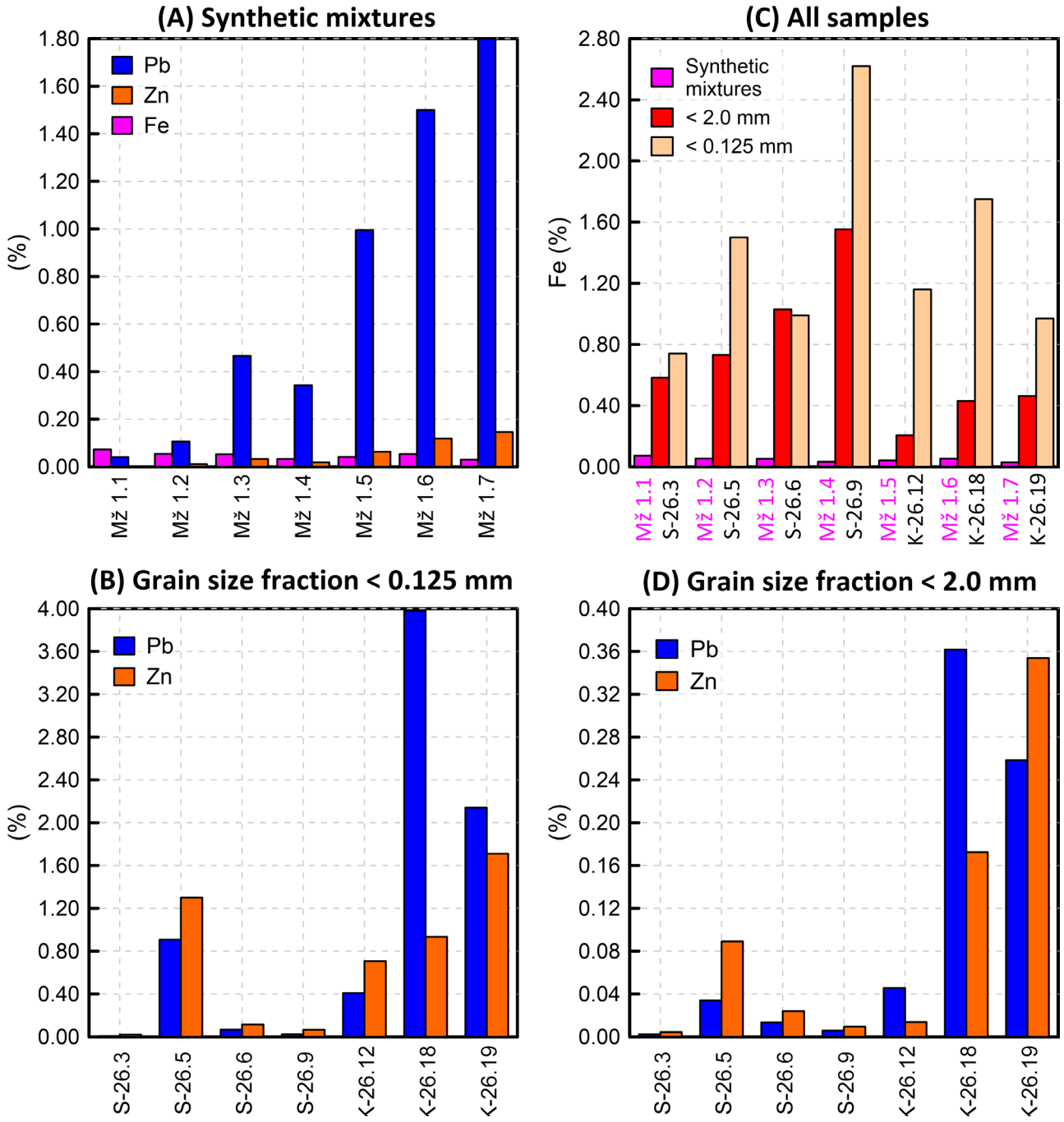

Fig. 2. Geochemical characterization of synthetic mixtures (Mž-samples), mine waste material (K-samples), and impacted stream sediments (S-samples). (A) Mass concentration of Pb, Zn and Fe (in %) of Mž-samples, SiO_2 not shown for brevity. (B) Mass concentration of Pb and Zn (in %) in the grain size fraction <0.125 mm of the K- and S- material samples (no SIP measurements). (C) Mass concentration of Fe (in %) in the Mž-samples, and K- and S- material samples of grain size fraction <0.125 mm and <2.0 mm. (D) Mass concentration of Pb and Zn (in %) in the grain size fraction <2.0 mm of the K- and S-material samples.

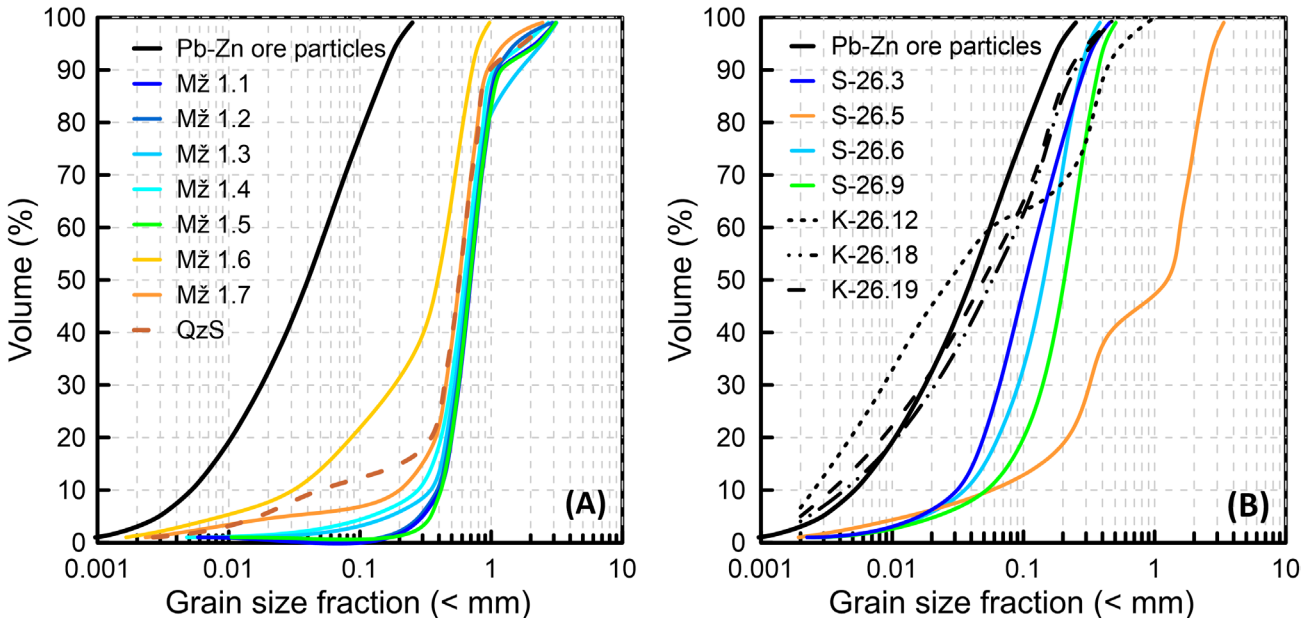

Fig. 3. Granulometric analysis of the composite samples of grain size fraction < 2.0 mm. (A) Grain size distribution of pure Pb-Zn ore particles, pure quartz sand (QzS), and synthetic samples (Mž-samples) made at different Pb-Zn ore particle concentrations (described in the main text). (B) Comparison of the grain size distribution among the Pb-Zn ore particles, mine waste material (K-samples) and stream contaminated sediment (S-samples). Concomitantly with geochemical analysis in the <0.125 mm fraction, the grain size fraction between 0.02 and 0.2 mm is the fraction where the highest concentrations of Pb-Zn metallic particles in both K- and S- material samples (<2.0 mm fraction) are expected.

SIP signatures and effect of salinity

According to Equations (4) and (5), SIP signatures can either be visualized in terms of conductivity magnitude and phase, i.e., $|\sigma^*|$ and $-\varphi$, or the corresponding real and imaginary conductivity, i.e., σ' and σ'', as per Equation (2) and (3), respectively. We start our discussion by looking at the whole spectrum of $-\varphi$ and/or σ'' aiming at visually distinguishing whether the signals show a flat spectrum or a polarization peak. This way, we can first identify the number of peaks and the corresponding peak frequencies, f_p, and then assess whether the polarization peaks are wide or narrow (see for example Fig. 1D).

In Figs. 4 and 5, we show the corrected spectra of the four components of the SIP signatures of samples K-26.18 and S-26.5 at full saturation with the $CaCl_2$ brine at different salinities (uncorrected raw spectra are shown in Fig. A3 of the Appendix). The measured responses show the effect of salinity by changes in the pore-water conductivity, σ_w, in both magnitude and shape of the spectra.

In both, K- and S- material samples, σ' and σ'' increase with salinity (i.e., with σ_w). As per Equation (5), the decrease in $-\varphi$ with salinity means that the increase in σ' is stronger than the increase in σ''. The $|\sigma^*|$ and σ' spectra are nearly flat within the measured frequency range, i.e., quite constant between the lowest and highest frequency. In the case of K-26.18, $-\varphi$ and σ'' spectra show a peak around $f_p = 125 - 250$ Hz, for the range of change of salinity. This shift of f_p towards higher frequencies with salinity (increase of electrolyte conductivity) is a typical behaviour in SIP spectra associated with metallic particles in porous media as suggested by the works of Placencia-Gómez and Slater (2016) and Hupfer et al. (2016).

In the S-26.5 material sample, the four components of the SIP signature (Fig. 5) are impacted by the salinity increase in a similar way as in the K-26.18 sample. However, the main distinction between K-26.18 and S-26.5 material samples, apart from the magnitudes, lies in the shape of the $-\varphi$ and σ'' spectra, and the peak frequencies f_p. In the S-26.5 sample, the high-frequency polarization was in magnitude lower than in the K-26.18 sample but affecting the measurements over a wider range of frequencies (i.e., starting from 100 Hz instead of 500 Hz, see Fig. A3 of the appendix). Consequently, in sample S-26.5 it was impossible to distinguish a peak polarization above the 100 Hz. However, after removing the effects in $i\omega C$, the phase shift is prevailing from 100 Hz onwards, so this is a clear indication that there might be some EDL polarization processes occurring at these high frequencies (Figs. 5-B, D). Following the works of Placencia-Gómez and Slater (2016) and Hupfer et al. (2016), in S-26.5 we only observe an increase of σ'' without a clear shift of f_p towards the higher frequencies (mainly impeded by the limited frequency range of measurements of our SIP instrument) with increasing σ_w (EC of the saturating

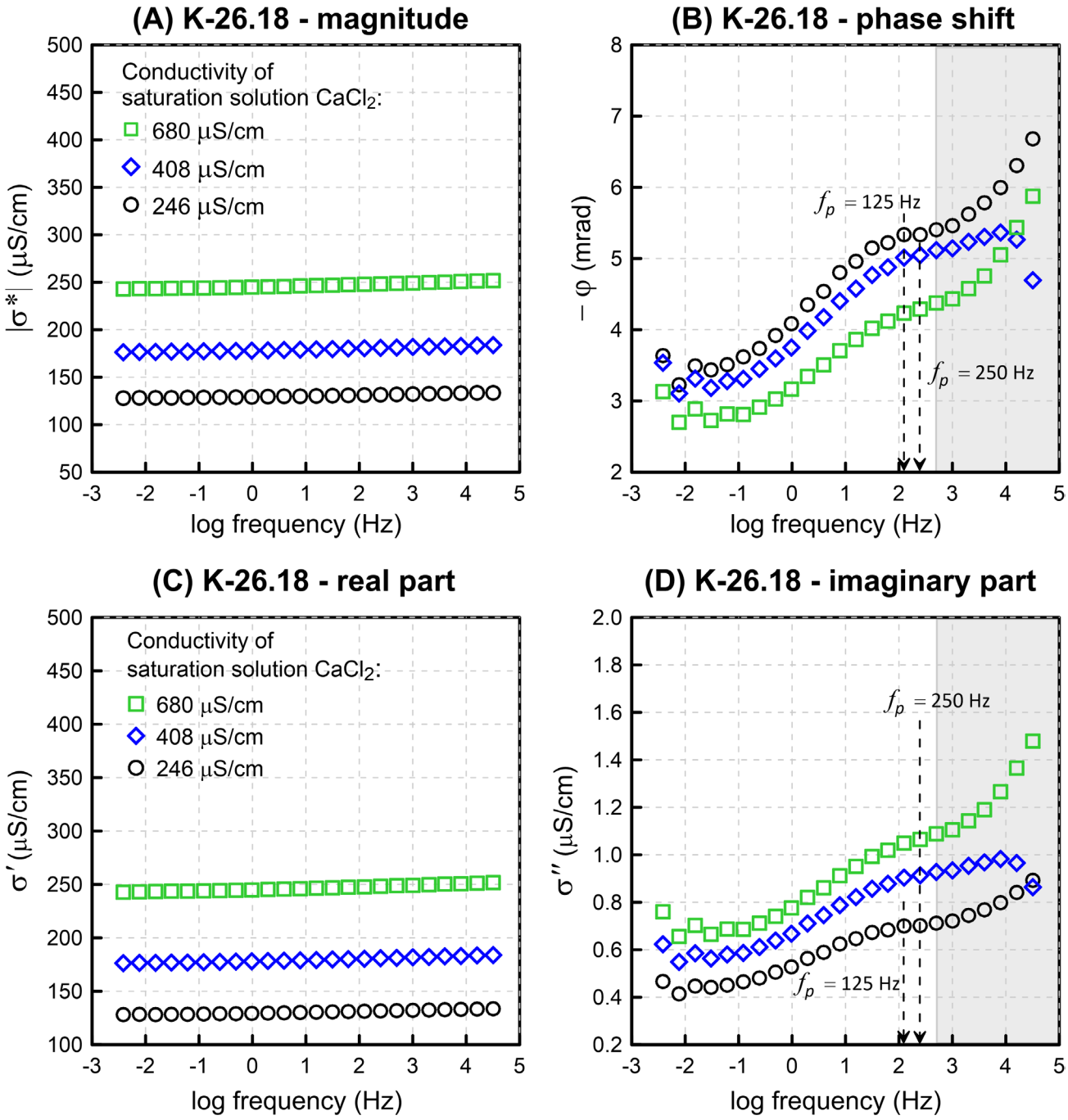

Fig. 4. SIP signatures of mine waste material sample K-26.18 (grain size fraction <2.0 mm) for different pore-water salinities under fully saturated conditions using $CaCl_2$ as the saturating solution. The shaded area depicts the range of frequencies where the high-frequency polarization trend ($i\omega C$) affected the measured raw spectra but was removed during processing (cf.Fig. A3 in the Appendix).

solution). By consequence, it is difficult to ensure that this polarization is fully associated with the presence of Pb and Zn particles (c.f., Fig. 2-D) and not influenced by the clay content. On the other hand, the clay content in S-26.5 (reported from the < 0.125 mm grain size fraction) is significantly smaller relative to the other S- material samples (Table 1) showing higher polarization magnitudes, σ'', than S-26.5 at the same salinity. Therefore, in the case of S-26.5 we can speculate that the significant increase in the σ'' magnitudes from 100 Hz onwards would be more likely associated with the metallic content than with the clays within the 20 % by volume of material in the <0.2 mm fraction sample as it shows the grain size analysis in Fig. 3-B.

Detection of metallic particles in the Mž-samples

In Fig. 6 we show the SIP signatures of synthetic mixtures (Mž-samples) at full saturation conditions with a $CaCl_2$ brine of EC = 680 µS/cm. Given the fact that the polarization of QzS (matrix) is null below 1 kHz and the high-frequency polarization trend is very low above 1 kHz (cf. Fig. A2), the

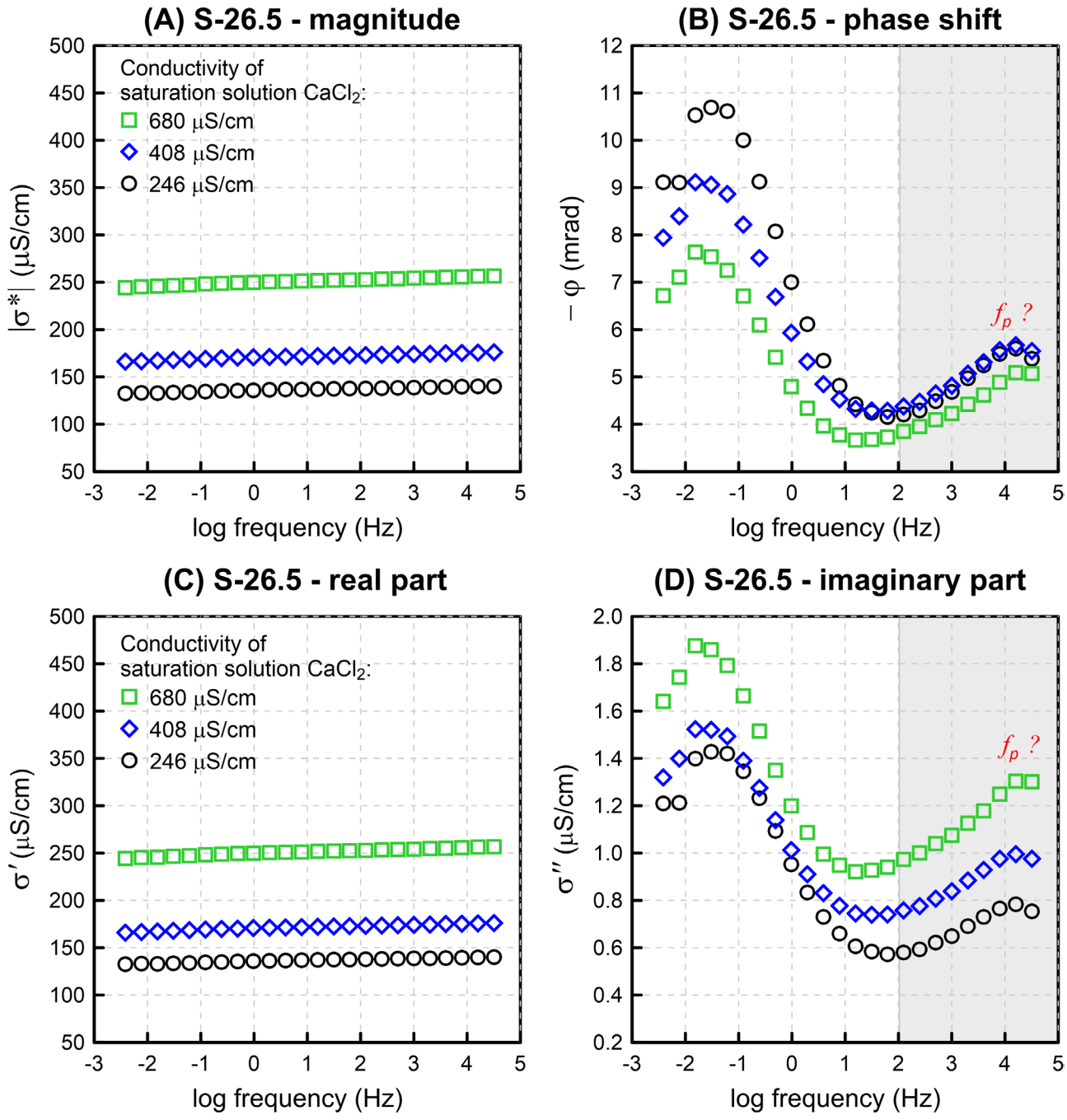

Fig. 5. SIP signatures of stream sediment sample S-26.5 (grain size fraction <2.0 mm) for different pore-water salinities under fully saturated conditions using $CaCl_2$ as the saturating solution. The shaded area depicts the range of frequencies where the high-frequency polarization trend ($i\omega C$) affected the measurements but was removed during processing (see Fig. A3 in the Appendix for the uncorrected raw spectra).

strong polarization peak observed in the σ'' and $-\varphi$ spectra at fp = 500 Hz can be attributed to the presence of the Pb-Zn ore particles. All four components of the complex conductivity increase in magnitude with the mass % concentration of the Pb-Zn ore particles in the samples. We note that the shape of both the peak in the $-\varphi$ and σ'' spectra along with the broadness of transition zone in the σ' spectra, are more like those spectra obtained when oxidation-reduction reactions at the surface of the metallic mineral are considered (cf. Fig. 1). Overall, results in Fig. 6 clearly show that the Pb-Zn ore particles (grain size fraction from 0.02 mm to 0.2 mm) from the Mežica mine disseminated in a non-polarisable matrix are detectable in the frequency range from 100 Hz to 1 kHz from both $-\varphi$ and σ''. In all mixtures, the high-frequency polarization trend ($i\omega C$) was insignificant relative to the electrochemical polarization at the surfaces of Pb-Zn ore (metallic) particles. Our results for sample Mž-1.3 at 2 vol. % ore (or its equivalent 4.28 mass % ore) are consistent with those of Hupfer et al. (2016) for their sample composed of medium galena, ranging in grain size from 0.061 mm to 0.1 mm

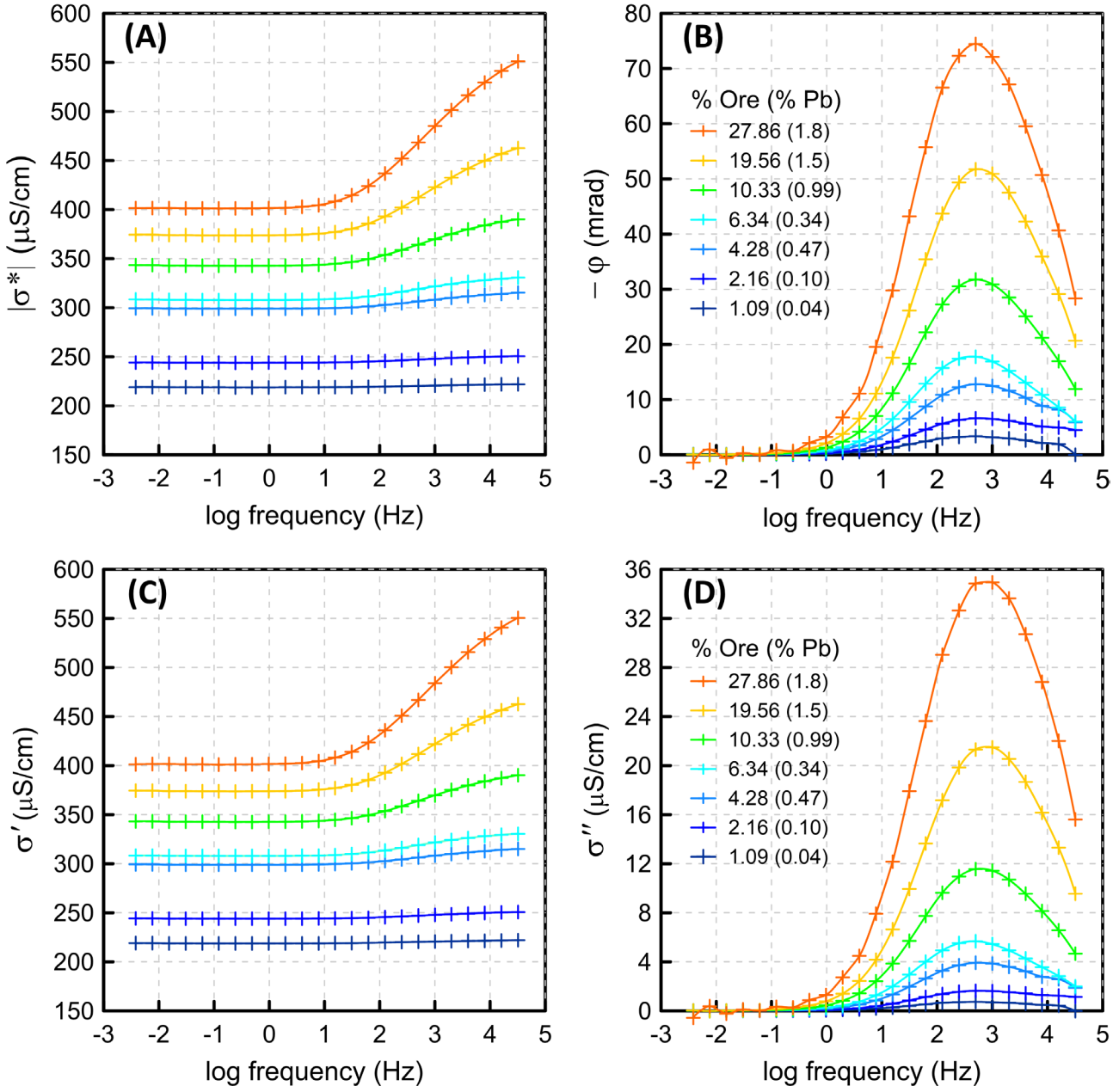

Fig. 6. SIP signature of the Mž-samples for varying concentrations of Pb-Zn ore particles in mass % and mass % of Pb estimated by XRF measurements (numbers in parenthesis) saturated with a brine of $CaCl_2$ at EC = 687 µS/cm. (A) magnitude of complex conductivity, (B) phase shift, (C) real part, and (D) imaginary part. The concentration of ore is given in vol. % in Table 2.

(their Table 1 and Fig. 5). They report for 2 vol. % of medium galena mixed in a silica sand matrix saturated with a porewater conductivity at 750 µS/cm, $-\varphi_p$ and σ''_p values at f_p = 1000 – 1580 Hz, of about 20 – 23 mrad and ≈ 4 µS/cm, and σ' values between 175 and 200 µS/cm, respectively. Whereas in our case we found $-\varphi_p \approx 13$ mrad, and $\sigma''_p \approx 4$ µS/cm occurring at f_p = 500 Hz, along with σ' values between 300 and 315 µS/cm, using a saturation brine at $EC/\sigma_w = 680$ µS/cm. This comparison suggests that coarse Pb-Zn particles, e.g., from 0.1 mm to 0.2 mm size fraction, governs the EDL's polarization in the Mž-samples.

Detection of metallic particles in the K- and S-material samples (<2.0 mm fraction)

In Fig. 7 and 8, we contrast the SIP signatures of the K- and S- material samples (grain-size fraction <2.0 mm) with those of the Mž-samples Mž-1.1 (1.09 mass % ore particles) and Mž-1.2 (2.16 mass % ore particles). We observe a clear increase in the magnitudes of $-\varphi$ and σ'' in the K- and S- material samples from about 1 Hz onwards (Fig. 7-B, D) and 10 Hz onwards (Fig. 8-B, D), respectively, that match with the frequency range between 10 Hz and 10 kHz, in which $-\varphi$ and σ'' show a distinct peak in the two reference Mž-samples (the shaded areas in Fig. 7 and Fig. 8). Based on the

results of XRF measurements (cf. Fig. 2-C, D), and the moderate content of silt and clay in the K-material samples (10 – 17 % in the <0.125 mm fraction, cf. Table 1), we interpret the high-frequency increase of $-\varphi$ and σ'' for the K-material samples to be mainly associated with the presence of fine grained Pb-Zn ore particles, fine Fe-rich particles, and to a lesser extent with the silt and clay content. In contrast, for some S-material samples, the increase in $-\varphi$ and σ'' from 10 Hz onwards might be partially associated with the high silt and clay content, particularly in samples S-26.3 and S-26.6 with a silt and clay content of 31.51 % and 31.6 %, respectively (cf. Table 1). According to the granulometric analysis (cf. Fig. 3 and Table 1), SIP spectra in Fig. 7 and Fig. 8 suggests that the increase in $-\varphi$ and σ'' of K-material samples from 1 Hz onwards and from 10 Hz onwards for the S-material samples, is associated with Fe-Pb-Zn metallic particles of grain size fraction <0.2 mm as in the two reference Mž-samples, possibly overlapping with the influence of silt and clay (<0.125 mm fraction); the influence of fine sand with a grain size fraction between 0.2 mm and 0.125 mm is neglected relative to that of the silt and clay fraction. To separate the influence of the silt/clay and metallic content in real geologic materials is challenging and requires a more detailed petrophysical, mineralogical and chemical analysis (see e.g., Ahmadi and Ghorbani, 2024) that we were limited to perform at this stage. To separate these two effects based on the SIP behaviour observed in the works of Placencia-Gómez and Slater (2016) and Hupfer et al. (2016) described above, has not been investigated in detail, for instance from mixtures of clay-ore in a matrix of silica or quartz sand. Additionally, in the case of the Mežica Pb-Zn mine waste material (K-material) and surrounding sediments (S-materials), the predominant host rock of Pb-Zn ore are carbonate rocks, so that investigations on the influence of such carbonate rocks as both the host rock matrix of ore and as sediments, on the SIP signatures must be investigated. At this stage, our interpretation of the potential influence of silt and clay effects, are overlapping with those of metallic content, is purely speculative based on qualitative particle size analysis. This analysis focuses on samples S-26.3, S-26.6, and S-26.9, where a larger silt and clay content would be expected according to the data in Table 1. The silt and clay content in these samples can reach concentrations up to ≈ 32 % and ≈ 12 % (i.e., the <0.125 mm fraction in the<2.0 mm grain size fraction of the samples). In the case of S-26.3 sample, the high silt and clay content (≈ 32 %) versus its particularly low content of Pb and Zn, suggests that $-\varphi$ and σ'' in this sample are not only influenced by Fe but also associated with its silt and clay content. Similarly, in samples S-26.6 and S-26.9, with ≈ 32 % and ≈ 12 % silt and clay content, along with partially high content in Fe, Pb and Zn, suggest that the high $-\varphi$ and σ'' magnitudes above 10 Hz, might be also associated with their silt and clay content. Going back to sample S-26.5, where the clay content is ≈ 8 % and the metallic content is high, the magnitudes of polarization, σ'', are quite similar to those in S-26.6 and S-26.9, indicating in this case the higher contribution linked to metallic particles than silts and clays to polarization.

Unfortunately, we were only able to capture a well-defined polarization peak, σ''_p, in sample K-26.18 (cf. Fig. 4), whereas in samples K-26.12 and K-26.19 (Fig. 7) we only observe a strong prevailing phase shift ($-\varphi$) and polarization (σ'') towards the high-frequency after performing correction, indicating the existence of a strong polarization other than that encompassed by the term $i\omega C$. Comparing the $-\varphi$ and σ'' spectra of K-26.18 and those of the Mž-samples, $-\varphi_p$ and σ''_p show up at a similar peak frequency, i.e., 250 Hz versus 500 Hz, as it shown in Fig. 7-B, D. This indicates that the presence of fine Fe-Pb-Zn metallic particles in sample K-26.18 is reflected by a peak in both the $-\varphi$ and σ'' spectra at f_p= 250 Hz (cf. Fig. 4). For the following analysis, which only applies to laboratory-scale SIP measurements, we therefore consider the polarization peak values at $f_p = 500$ Hz, as a proxy frequency to detect for the presence of metallic particles in both the K- and S-material samples. In the S-material samples, the increase in the $-\varphi$ and σ'' spectra with frequency from 10 Hz onwards (Fig. 8-B, D), fall within the same frequency range in which we observe the peaks in $-\varphi$ and σ'' for the two Mž-samples. This suggests that we were able to detect metallic particles in the S-material samples towards the higher frequencies, for instance at f_p= 500 Hz. The geochemical analysis in Fig. 2-C, shows relatively high Fe concentrations in the S-material samples (mass % in the <2.0 mm fraction), suggesting the IP-effect and polarization from 10 Hz onwards is influenced by the mass % concentration of Fe rather than that of Pb and Zn. The higher concentration of Fe in the S-material samples compared to the K-material samples (cf. Fig. 2-C), suggests the presence of natural sources rich in Fe in the surrounding areas of the Mežica mine waste deposits, so that the stream sediments show different mineralogical composition than the mine waste material (the mineralogical analysis is out of the scope

of this study). Magnitude, $|\sigma*|$, and real part, σ', of conductivity is larger in the K- than in the S-material samples. In both types of material, the $|\sigma*|$ and σ' values fall within the same order of magnitude as those of the two Mž-samples (Fig. 7-A, C and Fig. 8-A, C). Although $|\sigma*|$ and σ' cannot be used to detect the presence of metallic content, see for instance the same magnitude between Mž-1.2 and K-26.18 (Fig. 7), and between Mž-1.2 and S-26.5 (Fig. 8), the consistency in the orders of magnitude with the Mž-samples is a good qualitative indicator, which suggests that the SIP signatures of K- and S-material samples are associated with the metallic content in both types of materials.

On the other hand, we must make note that the strong polarization towards the lower frequencies in the S-material samples (Fig. 8-A, C) might not be associated with the presence of metallic particles, but rather associated with a coarse grain size fraction, mainly the 0.63 mm – 0.20 mm fraction, which apparently is the grain size fraction observable within the frequency range use for SIP measurements in all samples, with vol. % ranging from ≈ 30 % and ≈ 62 % in the S-samples, while in the K-samples between 18 % and ≈ 22 % (cf. Table 1). The coarse grain size fraction between 2.0 mm and 0.63 mm (coarse sand) in the K-samples is observable as a low-frequency increasing trend only in

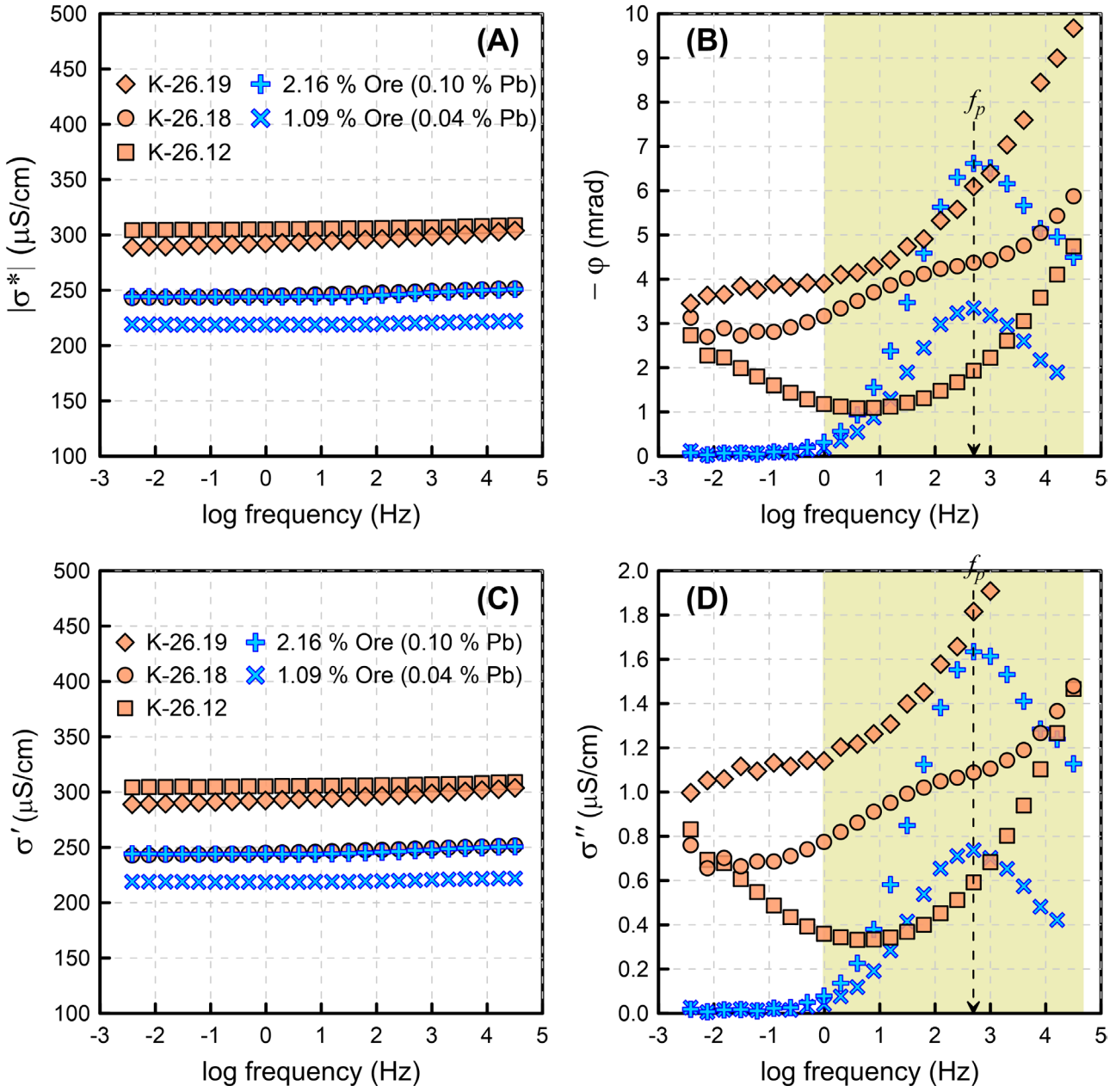

Fig. 7. Comparison of the SIP signatures of the Mž-1.1 (1.09 mass % of Pb-Zn ore particles) and Mž-1.2 sample (at 2.09 mass % of Pb-Zn ore particles) with those of the mine waste material samples K-26.12, K-26.18, and K-26.19, saturated with a solution of EC = 680 µS/cm. The shaded area in the $-\varphi$ and σ'' spectra indicates the range of frequency-increase of the IP effect, where metallic Pb-Zn-Fe particles in the grain-size fraction of <0.2 mm might be detected in the K-material as suggested by the σ''_p values at f_p= 500 Hz in synthetic mixtures (Mž-samples).

the K-26.12 sample, while in K-26.18 and K-26.19, the coarse sand is not detected, which is explained by the unintended small amounts used of this fraction at the moment of preparing the composite sample. However, this is not affecting our objectives because the concentration of the metallic content decreases significantly with the increase of the grain size fraction of the host material as observed in Fig. 2-C (<0.125 mm fraction) versus Fig. 2-D (<2.0 mm fraction). At this stage, we are not able to provide a more accurate geochemical analysis about the presence of metallic particles in specific coarse grain size fractions than those provided by XRF measurements shown in Fig. 2-D for the <2.0 mm fraction (note that the geochemical analysis of the <0.125 mm fraction, cf. Fig. 2-B, were done with a more accurate methodology as explained above). Based on the granulometric analysis, for instance in S-26.5, the 20 % by volume falls for the grain size fraction <0.2 mm, which is the upper limit of grain size of the Pb-Zn particles (cf. Fig. 3, black line). Therefore, it is likely that the presence of metallic particles (i.e., Fe-Pb-Zn rich particles, cf. Fig. 2-C, D) in the S- 26.5 sample is in the 20 % by volume, responsible of polarization observed towards the higher frequencies of SIP signatures (Fig. 8-B, D). The same interpretation suits for the other S-material

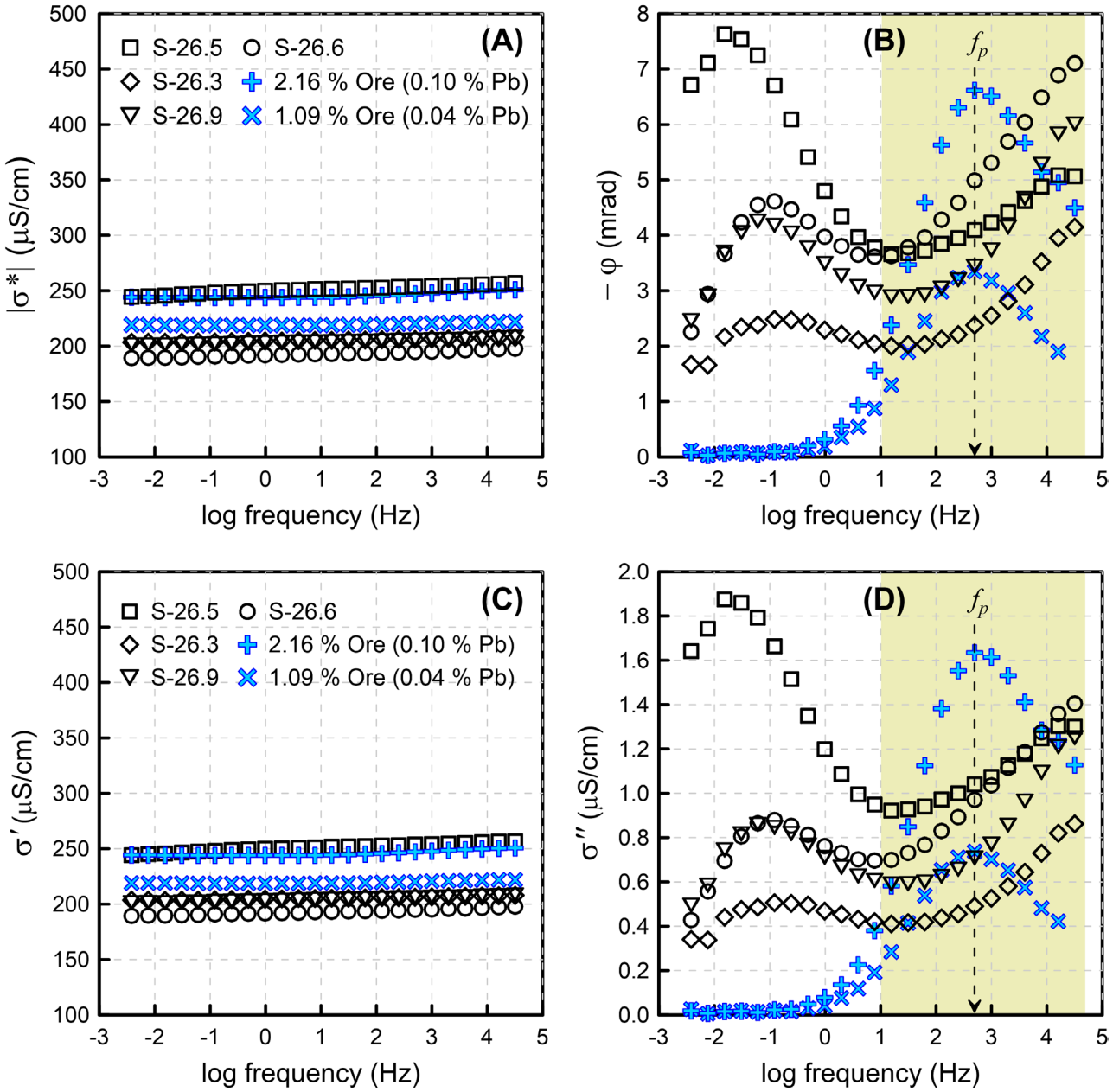

Fig. 8. Comparison of the SIP signatures of Mž-1.1 (1.09 mass % of Pb-Zn ore particles) and Mž-1.2 samples (at 2.09 mass % of Pb-Zn ore particles) with those of the stream-sediment samples S-26.3, S-26.5, S-26.6, and S-26.9, saturated with a solution of EC = 680 µS/cm. The shaded area in the $-\varphi$ and σ'' spectra indicates the range of frequency-increase of the IP effect, where metallic Fe-Pb-Zn particles in the grain size fraction <0.2 mm might be detected in the S-material as suggested by the σ''_p values at f_p= 500 Hz in synthetic mixtures (Mž-samples).

samples, that show up to 80 % and 50 % by volume of grain size fraction <0.2 mm (Fig. 3-B).

Relationships between polarization and chargeability and mass % of Pb, Zn, and Fe

In Fig. 9, we show the correlations between the polarization peak values σ''_p at f_p = 500 Hz, and the mass % concentration of Pb, Zn, and Fe, in both the K- and S- material samples (<2.0 mm fraction) and with the mass % concentration of ore, Pb and Zn in the Mž-samples (synthetic mixtures). Whereas in Fig. 10, we show the same correlations for chargeability values m_2. The results in Fig. 9-A, clearly show there is a strong influence of Fe on σ''_p for the K-samples alone (power-law relationship with exponent of 1.16), though the dependence of polarization on the entire ensemble of metallic content (m.c.), Fe, Pb, and Zn, can also be described fairly well (R^2 = 0.86) by a linear relationship (Fig. 9-B). In the case of the S-samples, the correlation σ''_p - Fe shows an inflection point with increasing the Fe concentration (Fig. 9-A), whereas for the correlation σ''_p - Pb, Zn follows a power-law relationship with exponent 0.31 and a coefficient of determination of R^2 = 0.88 (Fig. 9-C). We note that the R^2 values were higher for the power law fits than for linear fits in most cases, except for the K-samples in Fig. 9-B. The correlations between σ''_p and ore and between σ''_p and geochemical composition for the Mž-samples (Fig. 9-D, E, F), are shown for comparison and to illustrate the strong relationship between polarization magnitude and metallic particle concentration. As expected, the power-law relationships in the Mž-samples (synthetic mixtures), were close to a linear relationship for σ''_p- ore and σ''_p - Pb, with exponents 1.19 and 0.96, whereas for σ''_p - Zn the exponent was 0.38, showing in all three cases high R^2 values. The correlations shown in Fig. 9-D, show how one element, composing the ore particles, could exert greater relative influence on σ''_p than others, for instance in the order Pb > Zn > Fe as a function of its relative concentration. This is not surprising because Pb and Zn come from different sulphide minerals, mostly galena and sphalerite, with one dominant over the others. Whereas Fig. 9-E, F,

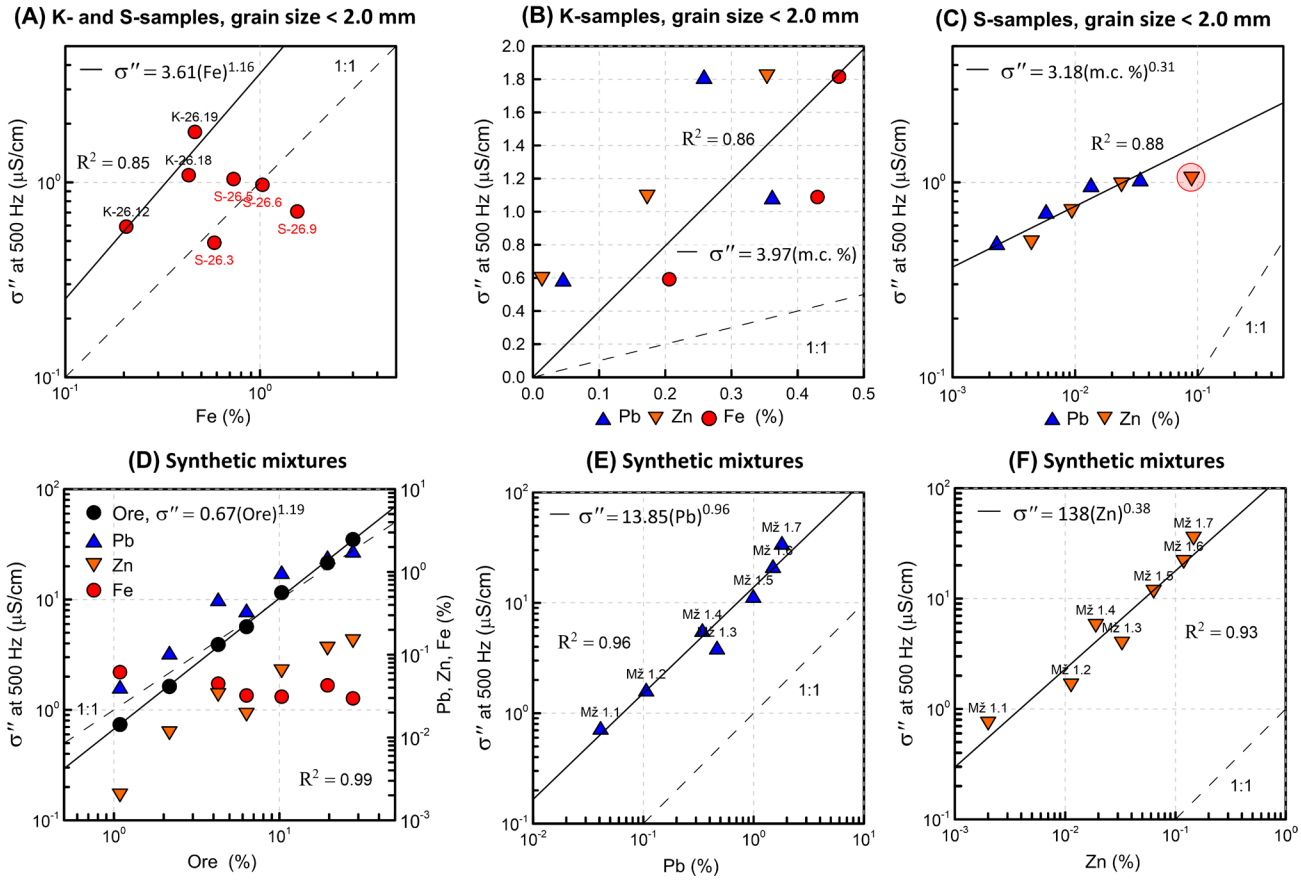

Fig. 9. Correlation between polarization peak values, σ''_p, at 500 Hz (f_p) and mass concentration (%) of major elements (geochemical composition) in the K- and S- material samples and Mž-samples for comparison. (A) Power-law relationship σ''_p – Fe for the K-material samples and inflection trend σ''_p – Fe for the S-material samples. (B) Linear relationship σ''_p – Pb, Zn, and Fe (the entire metallic content, m. c.) for the K-samples. (C) Power-law relationship σ''_p – Pb, Zn for the S-samples (outliers circled in red). (D) Power-law relationship σ'' – ore, and ore - mass % (concentration) of Pb, Zn and Fe in the Mž-samples (synthetic mixtures). (E) and (F) power-law relationship σ''_p – Pb, and σ''_p – Zn, for Mž- samples. The 1:1 ratio curve is shown as a guide.

clearly show the relative influence from every geochemical element correlates well with σ''_p. This analysis becomes important when we look at the S-samples. In this type of material, and neglecting for a while the clay content, the much higher mass % concentration of Fe than Pb and Zn does not appear to influence the σ''_p magnitudes and it is rather the Pb and Zn that seem to influence the polarization most (Fig. 9-A, C). Similarly, correlations between chargeability, m_2, and the elemental geochemical composition for the K- and S- material samples (Fig. 10-A, B, C), can be approximated by linear relationships, if two outliers are excluded from the fit. For the linear relationship m_2 – Fe, we considered both the K- and S- material samples all together to emphasize the sensitivity of chargeability to metallic content, i.e., Fe, that was found in very high mass % concentration relative to Pb and Zn in the S-samples. In the case of K-samples, and considering two outliers, the linear relationship m_2 – Fe, Pb, and Zn (m.c.) shows the same R^2 value (0.86) than for the linear relationship σ''_p - Fe, Pb, and Zn, whereas in the case of S-samples, the linear relationship m_2 – Pb, Zn, shown the smallest R^2 = 0.78. For the synthetic Mž-samples (Fig. 10-D, E, F), we observe again a good linear relationship between chargeability m_2 and the mass % of Pb-Zn ore particles, as well as between m_2 and Pb and Zn mass %. In the latter case, results suggest a stronger (more than the 1:1 ratio with coefficient 1.33) linear relationship m_2 – Zn than m_2 – Pb (lower than the 1:1 ratio with coefficient 0.1). Again, this result turns interesting in the sense that one would like to determine the influence of specific geochemical composition or element on the chargeability. The relationships shown in Fig. 10-E, F, suggests that more investigations on the Pb:Zn:Fe ratio are needed to provide reliable conclusions about their individual contribution to the IP effect, where one should avoid not considering the level of reactivity of each mineral or element. Nevertheless, a very rough analysis to separate the influence of Pb and Zn on the SIP signatures, can be made based on the percentage concentration of each element. For example, in the Mežica Pb-Zn ore particles, is the Pb (galena) that governs the chemical composition

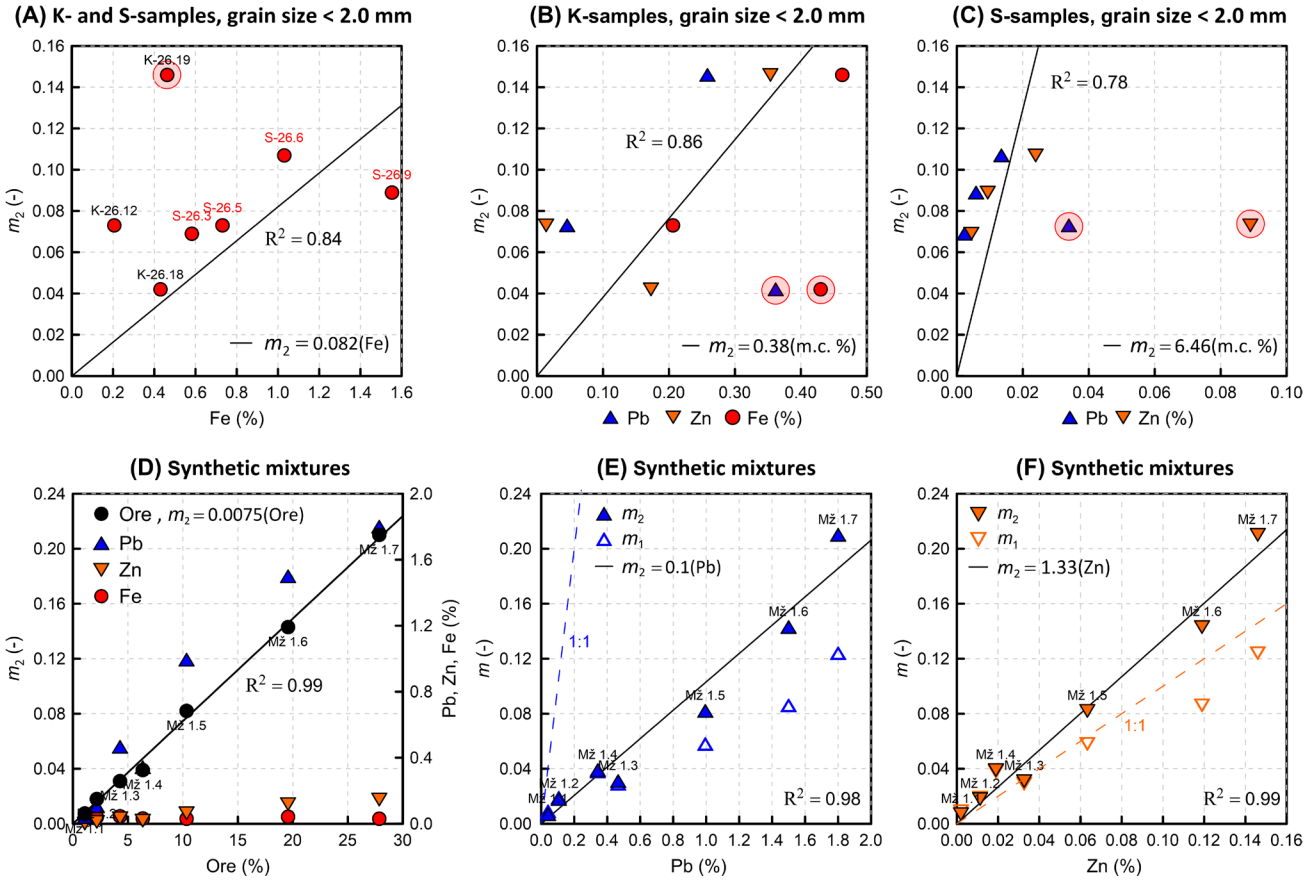

Fig. 10. Correlations between chargeability values, m_2, and the mass concentration (%) of major elements (geochemical composition) in the K- and S-material samples and Mž-samples for comparison. (A) Linear relationship m_2 – Fe for the K- and S- material samples all together (outliers circled in red). (B) Linear relationship m_2– Pb, Zn, and Fe (the entire metallic content, m. c.) for the K-samples (outliers circled in red). (C) Lineal relationship m_2 – Pb, Zn for the S-samples (outliers circled in red). (D) Lineal relationship m_2 – ore, and ore - mass % (concentration) of Pb, Zn and Fe in the Mž-samples (synthetic mixtures). (E) and (F) Lineal relationship m_2 – Pb, m_2 – Zn, and m_1 – Pb, m_1 – Zn (for comparison) for the Mž-samples. The 1:1 ratio curve is shown as a guide.

of this ore and therefore, based on this, we can diagnose a greater influence of Pb over Zn on both polarization and chargeability, both m_1 and m_2. On the other hand, the concentration of Fe is pretty the same in all the Mž-samples as seen in Fig. 9-D, so that its contribution to chargeability, as to polarization, is only significant at low ore concentration in mass % (e.g., $\leq$ 2 %) and minimal otherwise relative to Pb and Zn, respectively. Statistical analysis to validate the correlations in Fig. 9 and Fig. 10 was carried out. Results are shown in the Appendix for both the polarization peak values, σ''_p, and chargeability, m_2. We provide the correlation matrix, and the corresponding p-values matrix, separately for the K- and S- material samples and Mž-samples together, the K- and S- materials samples together, and the Mž-samples alone. The first statistical parameter shows there is no correlation between the SIP parameters and the Fe mass % concentration in all the cases, which is reflected in the p-values matrix resulting in non-rejected null-hypothesis. Otherwise, good correlation coefficients (consistent with R^2) were found in relation to the concentration of Pb and Zn when the outliers shown in Fig. 9-B,C and Fig. 10-B,C, are excluded. In general, excellent correlation was found in the case for K- and S-material samples together (Table A3 and Table B3 in the Appendix), specifically for the relationships $\sigma''p$ -Pb, $\sigma''p$ -Zn, m_2-Pb, and m_2-Zn, though the null-hypothesis was rejected only for $\sigma''p$ -Zn and m_2-Zn with p-values <0.05. In the case of the K- and S- material samples and Mž-samples all together and excluding outliers (Table A2 and Table B2 in the Appendix), the correlation coefficients were lower than in the previous case, but p-values were <0.05 for $\sigma''p$-Pb, m_2-Pb, and m_2-Zn.

Conclusions and perspectives

In this work, we have introduced the development of phase I of the geoelectrical laboratory (GEL) of GeoZS, showcasing an example of the unique sensitivity and potential usefulness of the SIP method to detect the presence of disseminated metallic minerals in geologic materials. This work showcases the relevance of laboratory-scale fundamental research to strengthen the ongoing applied research projects dealing with the geochemical characterization and environmental impact assessment of the Mežica Pb-Zn mine waste material and areas surrounding the waste deposits. In this work, we have mainly focused on the analysis of polarization (the imaginary part of measured complex conductivity) and chargeability values estimated from a novel modelling approach based on a double Cole-Cole relaxation model. Our results prove that these two already well-known SIP parameters are uniquely sensitive to electrochemical polarization and charge storage upon the EDLs developed on the surface of metallic particles, and therefore, useful proxies to detect the metallic content in both the K- and S-materials we have studied. In contrast, the magnitudes and real part of the measured complex conductivity, $|\sigma*|$ and σ', are limited to reflect changes in pore water conductivity (σ_w) linked to salinity variations. Nevertheless, at constant σ_w, these two also increase with the metallic content.

The geochemical composition of K- and S-materials suggests that the magnitudes of SIP signatures in the S-samples (<2.0 mm fraction) would be governed by Fe, Zn and Pb mass concentrations due to significantly higher concentrations of Fe than Pb and Zn. However, the higher concentrations of Pb and Zn observed in the <0.125 mm fraction of the mine waste material and sample S-26.5 should not be discarded from future SIP analysis as the volume of this fraction comprised in the <2.0 mm fraction is very significant, mainly in the S-samples as was shown by the granulometric analysis. The analysis of polarization peaks (σ''_p) and chargeability values (m_2), was useful to sense the influence of geochemical composition (Fe, Pb, and Zn, as the chemical elements with the highest concentration measured in all samples), in the SIP response of S-samples and K-samples, as well as in the Mežica Pb-Zn ore particles (Mž-samples), showing both in most of cases a positive linear dependence. Statistical analysis results validated the relationships between SIP parameters and geochemical data are statistically significant, rejecting the null-hypothesis. Nevertheless, they show there is no correlation between both the σ''_p and m_2 and the Fe content (in mass %) in all the cases, reflected by p-values much larger than the limit at 0.05, indicating the relationships shown in Fig. 9 and Fig. 10, are not statistically significant. We must note that the number of samples in this study is very small, so that a greater number of samples is needed to make a more accurate statistical analysis. However, the statistical analysis in the Mž-samples alone, where the content of Pb and Zn increase with the mass % of ore from sample Mž.1 to Mž.1.8, and the Fe content is small and quite constant in all the Mž-samples, is a good example to visualize the excellent correlation, statistically significant, between σ''_p and m_2, and the content of Pb and Zn, as well as the lack of a correlation with Fe.

Within the perspectives of monitoring the en-

vironmental impact of Mežica mine waste deposits, in Part II of this series, dedicated to metallic particles, we will present experimental work on synthetic mixtures of carbonates (limestone and dolomite) with the Mežica Pb-Zn ore particles at different grain size fractions, addressing the effects in the SIP signatures associated with changes in the pore water (electrolyte) conductivity as a potential way to discriminate the IP-effect of metallic contents from those associated with the clay content in both the K- and S- material samples. With this new set of experimental work, we expect to supplement and reinforce the results of this Part I, as well as to collect more data for statistical analysis. In Part II, we will analyse the relevance of the relaxation time (τ) and its distribution across the SIP spectrum, as well as the behaviour of the other Cole-Cole fitting parameters to characterize the geologic materials under study.

Part III, and the last part of this series, will be dedicated to integrate our SIP research work at the laboratory scale with dc-resistivity and time-domain IP measurements performed in two Mežica Pb-Zn mine waste deposits. Our goals in Part III, will be focused on collecting sufficient geophysical-geochemical data at both laboratory and field scale to find the scale factors that link the polarizability (σ'') measured from SIP and estimated m_2 SIP modelling parameter from Cole-Cole based models from samples, and the measured chargeability (M) from TDIP measurements at field scale. We believe that a multiscale analysis is missing, which is required to finally propose an approach for the estimation of the volumetric content of metallic particles from geophysical measurements and modelling parameters. We expect at the end of our investigation to provide an integrated approach useful for better management and characterization of the Mežica Pb-Zn mine waste deposits and their environmental impact on the surrounding areas.

Acknowledgements

This study was co-funded by the Slovenian Research and Innovation Agency (ARIS) in the frame of the "GEL project" (co-funded by ARIS within the framework of the Developmental funding pillar), the research programmes "Groundwater and Geochemistry" (P1-0020) and "Regional Geology" (P1-0011), as well as the research project "A holistic approach to the Earth surface processes driven by extreme weather events - ExtremEarth" (J7-60124). We express our sincere gratitude to Lee Slater and an anonymous reviewer for their comments and suggestions, which significantly improved our work. We acknowledge Lovro Rupar (Geological Survey of Slovenia) for translation to Slovenian language.

References

Abdel Aal, G.Z., Atekwana, E.A., Slater, L.D. & Atekwana, E.A.2004: Effects of microbial processes on electrolytic and interfacial electrical properties of unconsolidated sediments. Geophys. Res. Lett., 31/12: L12505. https://doi.org/10.1029/2004GL020030

Abdulsamad, F., Florsch, N. & Camerlynck, C. 2017: Spectral induced polarization in a sandy medium containing semiconductor materials: experimental results and numerical modelling of the polarization mechanism. Near Surface Geophysics, 15: 669–683.Ahmadi, S. & Ghorbani, A. 2024: Spectral Induced Polarization Response of Clay Rock Samples with a High Value of Pyrite. Journal of Analytical and Numerical Methods in Mining Engineering, 13/37: 21–39. https:/doi.org/10.22034/ANM.2023.20211.1598

Binley, A. & Slater, L. 2020: Resistivity and Induced Polarization: Theory and Applications to the Near-Surface Earth. Cambridge University Press: 388 p.

Binley, A., Slater, L.D., Fukes, M. & Cassiani, G. 2005: Relationship between spectral induced polarization and hydraulic properties of saturated and unsaturated sandstone. Water Resources Research, 41: W12417. https://doi.org/10.1029/2005WR004202

Bücker, M., Flores-Orozco, A. & Kemna, A. 2018: Electrochemical polarization around metallic particles - Part 1: The role of diffuse-layer and volume-diffusion relaxation. Geophysics, 83/4: E203-E217. https://doi.org/10.1190/geo2017-0401.1

Bücker, M., Undorf, S., Flores-Orozco, A. & Kemna, A. 2019: Electrochemical polarization around metallic particles — Part 2: The role of diffuse-surface charge. Geophysics, 84/2: E57–E73. http://dx.doi.org/10.1190/geo2018-0150.1.

Chuprinko, D. & Titov, K. 2017: Influence of mineral composition on spectral induced polarization in sediments. Geophys. J. Int. 209/1: 186–191. https://doi.org/10.1093/gji/ggx018

Ehosioke, S., Garré, S., Huisman, J. A., Zimmermann, E., Placencia-Gómez, E., Javaux, M. & Nguyen, F. 2023: Spectroscopic approach toward unravelling the electrical signature of

roots. Journal of Geophysical Research: Biogeosciences, 128: e2022JG007281. https://doi.org/10.1029/2022JG007281

Ehosioke, S., Nguyen, F., Rao, S., Kremer, T., Placencia-Gómez, E., Huisman, J. A., Kemna, A., Javaux, M. & Garré, S. 2020: Sensing the electrical properties of roots: A review. Vadose Zone Journal, 19: e20082. https://doi.org/10.1002/vzj2.20082

Florsch, N., Camerlynck, C. & Revil, A. 2014: Inversion of generalized relaxation time distributions with optimized damping parameter. Journal of Applied Geophysics, 109: 119–132. https://doi.org/10.1016/j.jappgeo.2014.07.013

Gosar, M., Šajn, R., Miler, M., Burger, A. & Bavec, Š. 2020: Overview of existing information on important closed (or in closing phase) and abandoned mining waste sites and related mines in Slovenia. Geologija, 63/2: 221–250. https://doi.org/10.5474/geologija.2020.018

Gosar, M., Bavec, Š., Miler, M. & Gaberšek, M. 2024: Contents of potentially toxic elements in sediments and waters of the Meža river and its tributaries draining mine waste deposits. Geologija, 67/1: 41–61. https://doi.org/10.5474/geologija.2024.003

Gurin, G., Tarasov, A., Ilyin, Y. & Titov, K. 2013: Time domain spectral induced polarization of disseminated electronic conductors: Laboratory data analysis through the Debye decomposition approach. Journal of Applied Geophysics, 98: 44–53. https://doi.org/10.1016/j.jappgeo.2013.07.008

Gurin, G., Titov, K., Ilyin, Y. & Tarasov, A. 2015: Induced polarization of disseminated electronically conductive minerals: A semi-empirical model. Geophysical Journal International, 200: 1555–1565. https://doi.org/10.1093/gji/ggu490.

Gurin, G., Ilyin, Y., Nilov, S., Ivanov, D., Kozlov, E. & Titov, K. 2018: Induced polarization of rocks containing pyrite: Interpretation based on X-ray computed tomography. Journal of Applied Geophysics, 154: 50–63. https://doi.org/10.1016/j.jappgeo.2018.04.019.

Hupfer, S., Martin, T., Weller, A., Günther, T., Kuhn, K., Ngninjio, V.D.N. & Noell, U. 2016: Polarization effects of unconsolidated sulphide-sand-mixtures. Journal of Applied Geophysics, 135:456–465. https://doi.org/10.1016/j.jappgeo.2015.12.003

Kessouri, P. et al. 2019: Induced polarization applied to biogeophysics: recent advances and prospects. Near Surface Geophysics, 17/6: 595–621. https://doi.org/10.1002/nsg.12072

Leroy, P. & Revil, A. 2009: A mechanistic model for the spectral induced polarization of clay materials. J. Geophys. Res., 114: B10202. https://doi.org/10.1029/2008JB006114

Leroy, P., Revil, A., Kemna, A., Cosenza, P. & Ghorbani, A. 2008: Complex conductivity of water-saturated packs of glass beads. J. Colloid Interface Sci., 321/1: 103–117. https://doi.org/10.1016/j.jcis.2007.12.031

Lewis, J. & Sjöstrom, J. 2010: Optimizing the experimental design of soil columns in saturated and unsaturated transport experiments. Journal of Contaminant Hydrology, 115: 1-13. https://doi.org/10.1016/j.jconhyd.2010.04.001

Maineult, A. 2016: Estimation of the electrical potential distribution along metallic casing from surface self-potential profile. Journal of Applied Geophysics, 129, 66-78.

Maineult, A., Leroy, P., Mendieta, A. & Jougnot, D. 2025a: A mechanistic model for the complex conductivity of clay materials. II. Comparison to experimental data. Geophysical Journal International, 241, 110-132. https://doi.org/10.1093/gji/ggae428

Maineult, A., Weller, A., Martin, T., Titov K. & Florsch, N. 2025b: 3D impedance networks simulate complex resistivity spectra of sand-pyrite-water mixtures. Geophysical Journal International, 24/3: 1–17. https://doi.org/10.1093/gji/ggaf269

Martin, T. & Günther, T. 2013: Complex Resistivity Tomography (CRT) for fungus detection on standing oak trees. European Journal of Forest Research, 132: 765–776. https://doi.org/10.1007/s10342-013-0711-4

Martin, T., Weller, A. & Behling, L. 2022: Desaturation effects of pyrite–sand mixtures on induced polarization signals. Geophysical Journal International, 228: 275–290.

Martin, T. & Weller, A. 2023: Superposition of induced polarization signals measured on pyrite–sand mixtures. Geophysical Journal International, 234: 699–711.

Mendieta, A., Jougnot, D., Leroy, P. & Maineult, A. 2021: Spectral induced polarization characterization of non-consolidated clays for varying salinities—an experimental study. J. Geophys. Res.: Solid Earth. 126/4: e2020JB021125. https://doi.org/10.1029/2020JB021125

Mendieta, A., Maineult, A., Leroy, P. & Jougnot, D. 2023: Spectral induced polarization of heterogeneous non-consolidated clays. Geophysical Journal International, 233: 436–447.

Miler, M., Bavec, Š. & Gosar, M. 2022: The envi-

ronmental impact of historical Pb-Zn mining waste deposits in Slovenia. J. Environ. Manag. 308: 114580. https://doi.org/10.1016/j.jenvman.2022.114580

Ntarlagiannis, D. & Ferguson, A. 2009: SIP response of artificial biofilms. Geophysics, 74/1: A1-A5. https://doi.org/10.1190/1.3031514

Ntarlagiannis, D., Yee, N. & Slater, L. 2005. On the low-frequency electrical polarization of bacterial cells in sands. Geophysical Research Letters, 32/24: L24402. https://doi.org/10.1029/2005GL024751

Peshtani, K., Weller, A. & Slater, L. 2024: Permeability and induced polarization of mudstones. Water Resour. Res., 60/8. https://doi.org/10.1029/2024WR037455

Placencia-Gómez, E., Parviainen, A., Slater, L. & Leveinen, J. 2015: Spectral induced polarization (SIP) response of mine tailings. J. Contam. Hydrol., 173: 8–24. https://doi.org/10.1016/j.jconhyd.2014.12.002

Placencia-Gómez, E. & Slater, D.L. 2016: On the pore water chemistry effect on spectral induced polarization measurements in the presence of pyrite. J. App. Geop., 135: 474–485. https://doi.org/10.1016/j.jappgeo.2015.11.001

Placencia-Gómez, E., Slater, L., Ntarlagiannis, D. & Binley, A. 2013: Laboratory SIP signatures associated with oxidation of disseminated metal sulfides. J. Contam. Hydrol., 148: 25–38. https://doi.org/10.1016/j.jconhyd.2013.02.007

Prodan, C., Mayo, F., Claycomb, J.R., Miller, J.H. & Benedik, M.J.2004: Low-frequency, low-field dielectric spectroscopy of living cell suspensions. J. Appl. Phys., 95: 3754–3756. https://doi.org/10.1063/1.1649455

Revil, A., Abdel Aal, G.Z., Atekwana, E.A., Mao, D. & Florsch, N. 2015a: Induced polarization response of porous media with metallic particles — Part 2: Comparison with a broad database of experimental data. Geophysics, 80/5: D539–D552. https://doi.org/10.1190/geo2014-0578.1

Revil, A., Florsch, N. & Mao, D. 2015b: Induced polarization response of porous media with metallic particles – Part 1: A theory for disseminated semiconductors. Geophysics, 80/5: D525–D538. https://doi.org/10.1190/geo2014-0577.1

Slater, L., Choi, J. & Wu, Y. 2005: Electrical properties of iron-sand columns: Implications for induced polarization investigation and performance monitoring of iron-wall barriers. Geophysics, 70/4: G87–G94. https://doi.org/10.1190/1.1990218

Slater, L., Ntarlagiannis, D. & Wishart, D. 2006: On the relationship between induced polarization and surface area in metal-sand and clay-sand mixtures. Geophysics, 71/2: A1–A5. https://doi.org/10.1190/1.2187707

Wong, J. 1979: An electrochemical model of the induced-polarization phenomenon in disseminated sulfide ores. Geophysics, 44/7: 1245–1265. https://doi.org/10.1190/1.1441005

Wu, Y., Hubbard, S., Williams, K.H. & Ajo-Franklin, J. 2010. On the complex conductivity signatures of calcite precipitation. Journal of Geophysical Research, 115/G2: G00G04. https://doi.org/10.1029/2009JG001129

Zimmermann, E., Kemna, A., Berwix, J., Glaas, W., Münch, H.M. & Huisman, J. A. 2008: A high-accuracy impedance spectrometer for measuring sediments with low polarizability.
Measurement Science and Technology, 19/10: 105603. https://doi.org/10.1088/0957-0233/19/10/105603

Zhang, C., Revil, A., Fujita, Y., Munakata-Marr, J. & Redden, G. 2014: Quadrature conductivity: A quantitative indicator of bacterial abundance in porous media. Geophysics, 79/6: D363–D375. https://doi.org/10.1190/geo2014-0107.1

Appendix

SIP measurement unit, experimental device and calibration

In Fig. A1, we show the SIP-COMPACT-S measurement unit, and the home-made experimental measurement device for SIP measurements in disturbed/undisturbed samples of geologic materials, whereas in Fig. 2A, we show the calibration measurements that validate the SIP measurement's reliability. We show the SIP response for the QzS fully saturated with the EC = 680 µS/cm $CaCl_2$ brine. The QzS shows very small (close to zero) values of $-\varphi$ and σ'' up to 1 kHz, increasing to 7 mrad or up to 2.4 µS/cm in σ''. The very small magnitudes of $-\varphi$ and σ'' spectra < 1 kHz reflect that the possible background polarization by the QzS used as matrix material in the synthetic mixtures is null. The increasing trend of $-\varphi$ and σ'' towards high frequencies (>1 kHz) are typical for SIP measurements, but it is recommended to target small polarization or $-\varphi$ magnitudes above 1 kHz during the calibration. We consider that the $-\varphi$ values below 7 mrad from 1 kHz onwards result from a good quality of potential electrodes, good contact resistance of electrodes with the electrolyte or agar, minimum influence of electronic parts in the instrument, and electromagnetic coupling effects between cables that might cause parasitic capacitances and thus affect the SIP signatures.

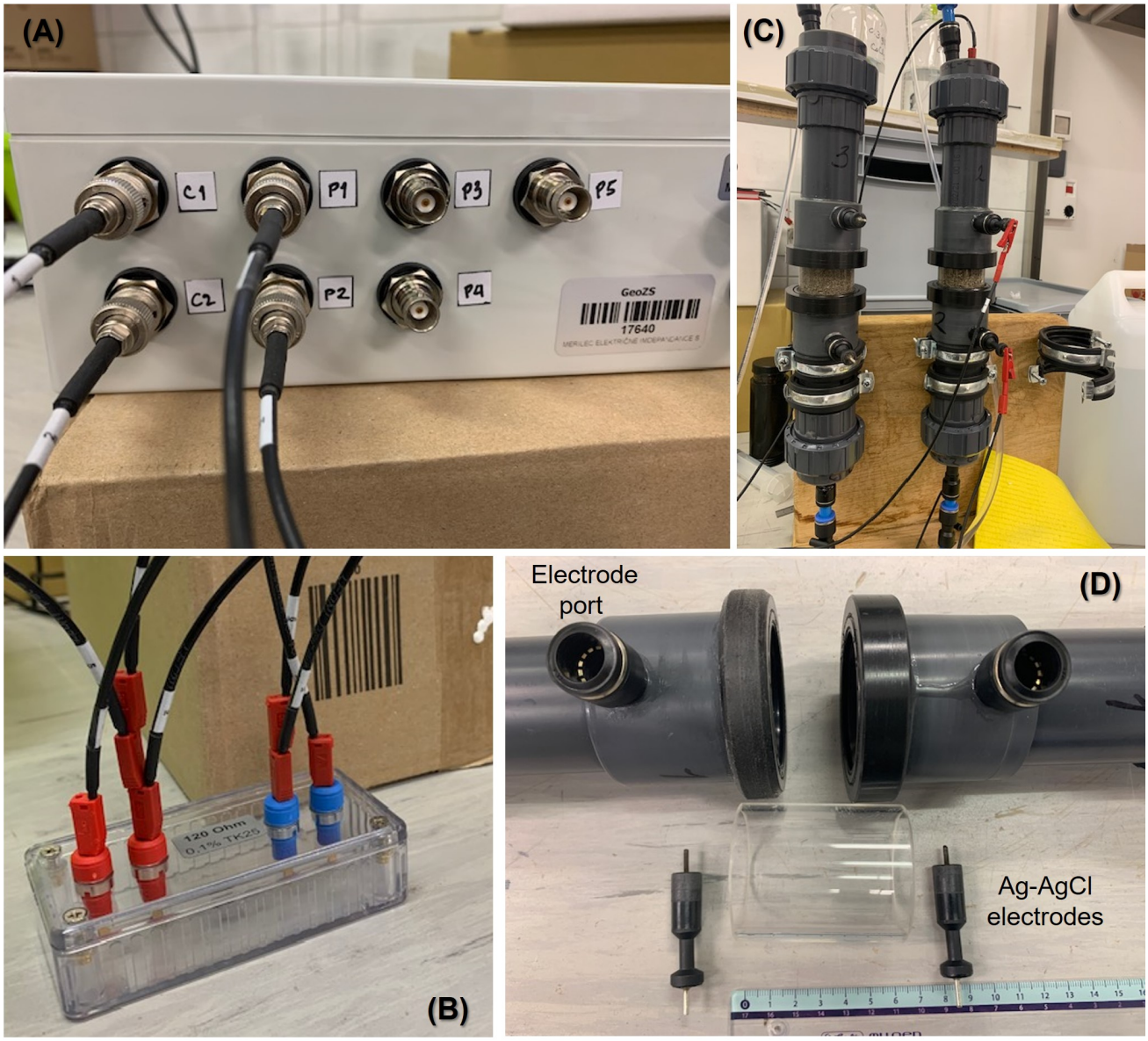

Fig. A1. Setup of experimental SIP measurements at the GEL of GeoZS. (A) SIP measurement unit, SIP-COMPACT-S, manufactured by Radic Research (Germany). (B) 120 Ohm reference resistor for calibration of the measurement unit. (C) Experimental SIP measurements on geologic material columns under fully saturated conditions. (D) Components of the experimental measurement device.

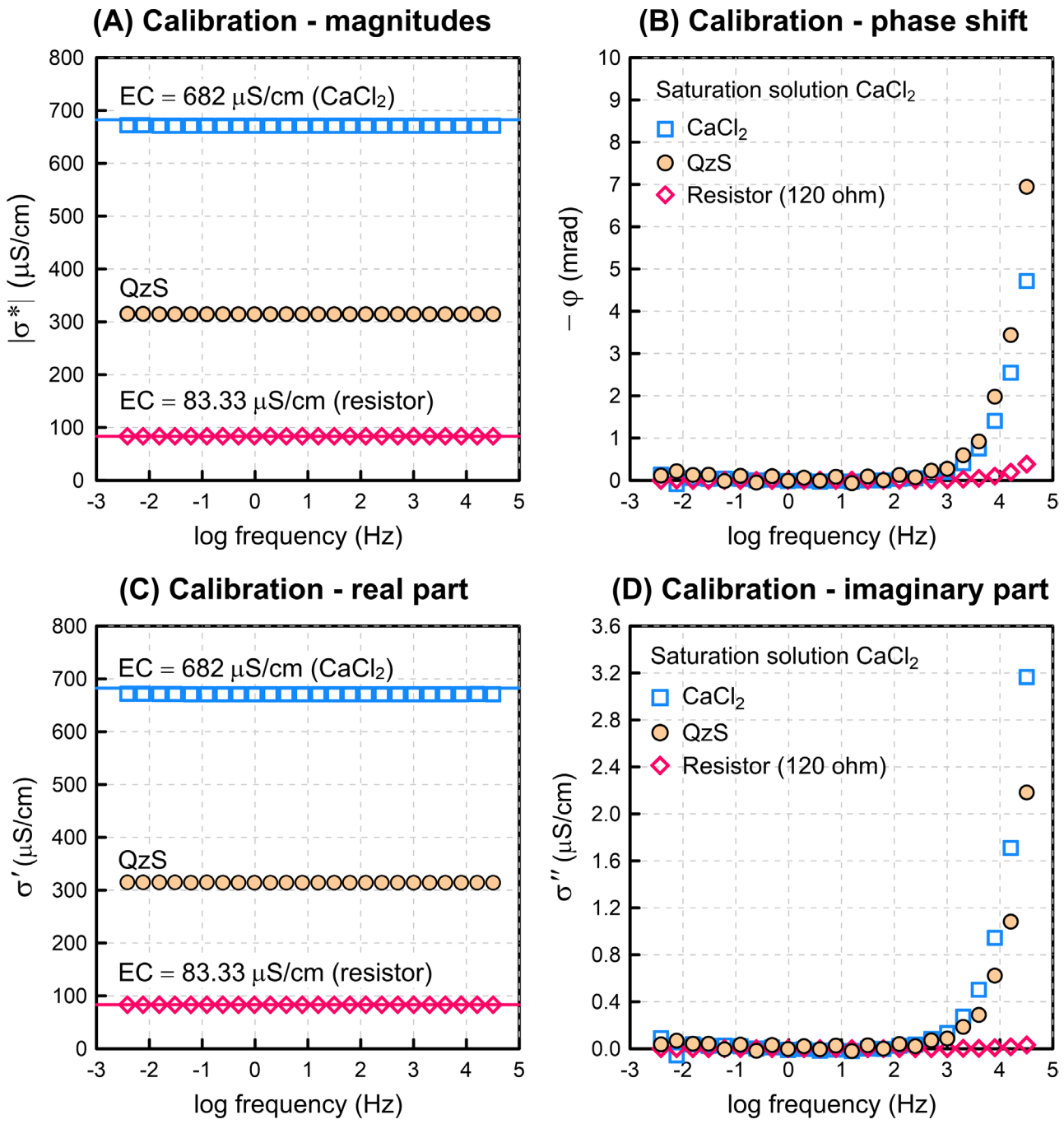

Fig. A2. Calibration results of the experimental measurement device and the SIP measurement unit. (A) magnitude of the complex conductivity, (B) phase shift, (C) real part, and (D) imaginary part of the complex conductivity (SIP spectra). Continuous lines depict the reference value of the electrical conductivity (EC) for the $CaCl_2$ brine alone measured with a regular bench-conductivity meter probe, and the EC for the 120 Ohm resistor (with geometric factor of 1 m). QzS stands for the quartz sand (saturated with the brine $CaCl_2$) used as the matrix in the Mž-samples. Symbol curves are the SIP measurements (raw data).

Correction of SIP signatures

The effects of undesired polarization in the SIP signatures are shown in detail in Fig. A3. We illustrate these effects for sample K-26.18 and S-26.5 associated with salinity variations. In sample K-26.18 the undesired polarization ($i\omega C$) begins to be visible from ≈500 Hz, which did not prevent the distinction of a polarization peak around f_p = 125 at the lowest salinity (EC = 246 µS/cm), but their removal was needed to distinguish better that the peak appears to stabilize at f_p = 250 Hz with increasing salinity (i.e., with the increase of σ_w). The undesired polarization effects, visualized as a high-frequency polarization trend in both the $-\varphi$ and σ'' spectra, were successfully removed in terms of the component defined as $i\omega C$ (Equation 7, in the text), resulting in a smoothed signature as shown in Fig. A3 for the three EC values of saturation solution. In the text, we only show the corrected spectra depicting by a shaded area the range of frequencies of affected measured data.

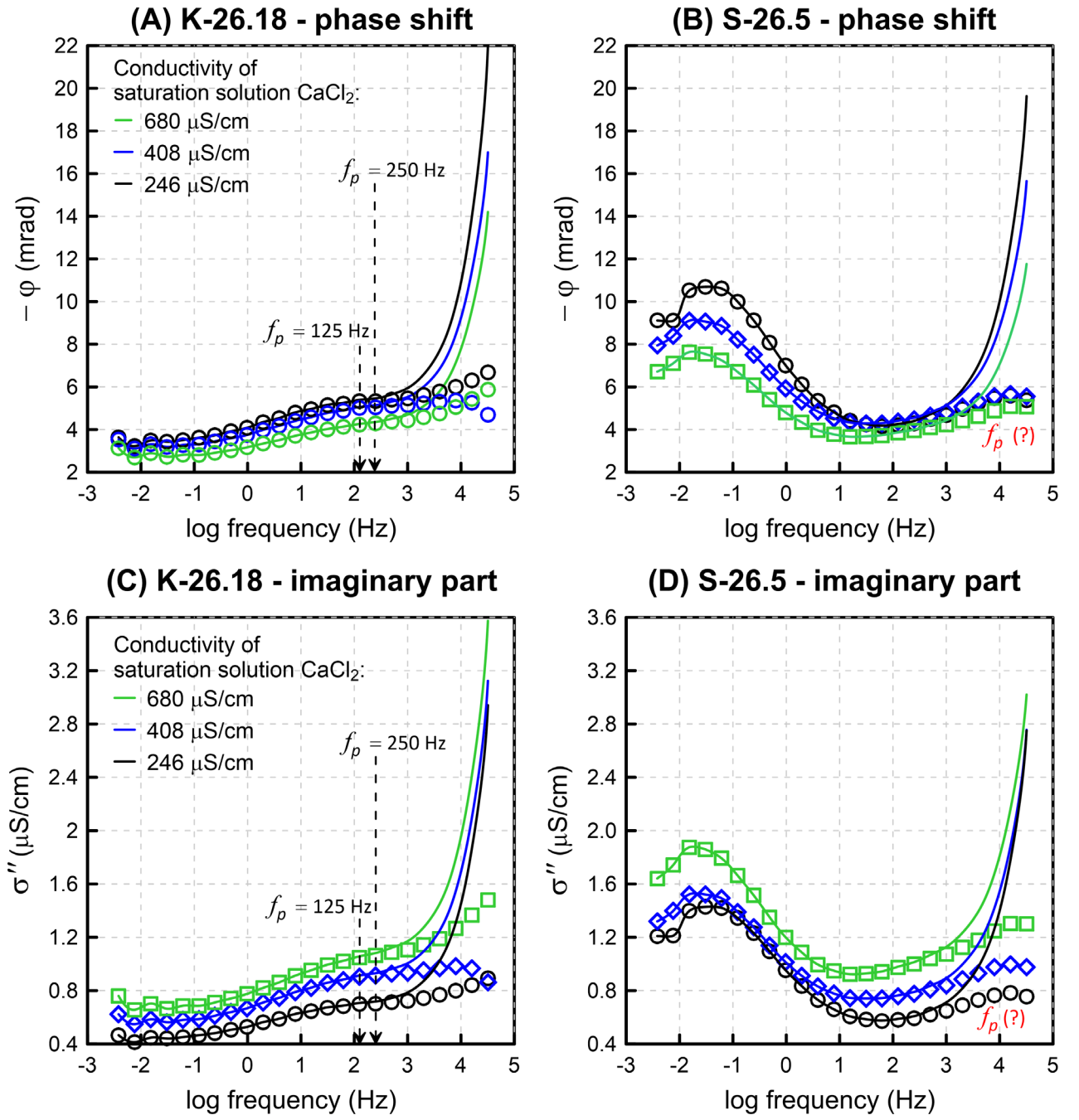

Fig. A3. Raw measurements (continuous line) and corrected (symbols) of phase shift ($-\varphi$) and polarization (σ'') spectra for the K- and S-materials associated with changes of salinity. The polarization peaks (σ'') and corresponding peak frequencies (f) in the sample K-26.18 were slightly affected by the high-frequency polarization trend ($i\omega C$) starting at ≈500 Hz. In contrast, for the sample S-26.5 it was impossible to distinguish a peak. However, after performing the correction process, yet a strong $-\varphi$ and polarization σ'' are visible towards the high frequencies.

Statistical analysis of correlations between σ''_p, m_2 and geochemical composition

Statistical data analysis was done by estimating the correlation coefficients matrix and the corresponding p-values matrix for testing the null hypothesis. Tables below show the results for the correlation between polarization at 500 Hz, σ''_p, chargeability, m_2, estimated by a double Cole-Cole fitting model, and metallic content in mass % of Pb, Zn and Fe measured by XRF in all the materials samples (K- and S- materials samples) and synthetic samples (Mž-samples). Although the reduced number of data (samples), results in Table A1, A2 and Table B1, B2 (for the case of the K- and S-material samples and synthetic Mž-samples all together) show there is a significant relationship between σ'', m_2 and the metallic content in mass % of Pb and Zn, that is consistent with the R^2 estimated from correlations shown in Fig. 9 and Fig. 10, respectively. The p-values < 0.05 for the correlations σ''_p-Pb, m_2-Pb and m_2-Zn, excluding outliers, shows that the corresponding relationships

are statistically significant. In contrast, for σ''_p-Fe, and m_2-Fe, there is a poor correlation accompanied by large p-values (>0.05) indicating there is no relationship between σ''_p, m_2 and Fe in the S-material samples and Mž synthetic mixtures (c.f., Fig. 9-A,C and Fig. 10-D). By excluding the outliers in the correlation plots shown in Fig. 9-B, C and Fig. 10-B, C, the correlation values for σ''_p-Zn, and m_2-Zn increase a little bit and the p-values are in general better for σ''_p-Zn, and m_2-Zn than for σ''_p-Pb, and m_2-Pb (Tables A2, A3 and Tables B2, B3). For comparison, in Table A4 and Table B4, we show the statistical results for the Mž-samples alone. In this case the correlation coefficient values were consistent with the R^2 in Fig. 9-E, F and Fig. 10-E, F, with high values for σ''_p-Pb, Zn, and m_2-Pb, Zn, indicating the excellent relationship, whereas for σ''_p-Fe, and m_2-Fe the correlation coefficients values are negative indicating a negative relationship. This is reflected in the p-values, showing the lowest p-values for the case of Pb and Zn, and very high values for Fe.

Table A1. Correlation coefficients for all materials and synthetic samples together.

	σ''_p	Pb	Zn	Fe
σ''_p	**1**	0.9631	0.2360	-0.4128
Pb	**0.9631**	**1**	0.3118	-0.4879
Zn	**0.2360**	**0.3118**	**1**	-0.0642
Fe	**-0.4128**	**-0.4879**	**-0.0642**	**1**
	m_2	Pb	Zn	Fe
m_2	**1**	0.6614	0.5525	0.1051
Pb	**0.6614**	**1**	0.3118	-0.4879
Zn	**0.5525**	**0.3118**	**1**	-0.0642
Fe	**0.1051**	**-0.4879**	**-0.0642**	**1**

Table B1. p-values for all materials and synthetic samples together.

	σ''_p	Pb	Zn	Fe
σ''_p	**1**	3.3e-08	0.4167	0.1424
Pb	**3.3e-08**	**1**	0.2778	0.0768
Zn	**0.4167**	**0.2778**	**1**	0.8274
Fe	**0.1424**	**0.0768**	**0.8274**	**1**
	m_2	Pb	Zn	Fe
m_2	**1**	0.0100	0.0405	0.7206
Pb	**0.0100**	**1**	0.2778	0.0768
Zn	**0.0405**	**0.2778**	**1**	0.8274
Fe	**0.7206**	**0.0768**	**0.8274**	**1**

Table A2. Correlation coefficients for all materials and synthetic samples together excluding the outliers shown in Fig. 9-B, C and Fig. 10-B, C.

	σ''_p	Pb	Zn	Fe
σ''_p	**1**	0.9632	0.2445	-0.3945
Pb	**0.9632**	**1**	0.3257	-0.4655
Zn	**0.2445**	**0.3257**	**1**	-0.0746
Fe	**-0.3945**	**-0.4655**	**-0.0746**	**1**
	m_2	Pb	Zn	Fe
m_2	**1**	0.6718	0.6539	0.1298
Pb	**0.6717**	**1**	0.3549	-0.4642
Zn	**0.6539**	**0.3549**	**1**	-0.0935
Fe	**0.1298**	**-0.4642**	**-0.0935**	**1**

Table B2. p-values for all materials and synthetic samples together excluding the outliersshowninFig. 9-B,C and Fig. 10-B,C.

	σ''_p	Pb	Zn	Fe
σ''_p	**1**	1.3e-07	0.4208	0.1822
Pb	**1.3e-07**	**1**	0.2775	0.1090
Zn	**0.4208**	**0.2775**	**1**	0.8085
Fe	**0.1822**	**0.1090**	**0.8085**	**1**
	m_2	Pb	Zn	Fe
m_2	**1**	0.0167	0.0211	0.6876
Pb	**0.0167**	**1**	0.2576	0.1285
Zn	**0.0211**	**0.2576**	**1**	0.7726
Fe	**0.6876**	**0.1285**	**0.7726**	**1**

Table A3. Correlation coefficients for K- and S-materials samples together excluding the outliers shown in Fig. 9-B, C and Fig. 10-B, C.

	σ''_p	Pb	Zn	Fe
σ''_p	**1**	0.6893	0.9499	-0.1766
Pb	**0.6893**	**1**	0.8048	-04668
Zn	**0.9499**	**0.8048**	**1**	-0.3659
Fe	**-0.1766**	**-04668**	**-0.3659**	**1**
	m_2	Pb	Zn	Fe
m_2	**1**	0.8504	0.8956	0.0010
Pb	**0.8504**	**1**	0.9888	-0.4150
Zn	**0.8956**	**0.9888**	**1**	-0.3157
Fe	**0.0010**	**-0.4150**	**-0.3157**	**1**

Table B3. p-values for K- and S-materials samples excluding the outliers shown in Fig. 9-B,C and Fig. 10-B,C.

	σ''_p	Pb	Zn	Fe
σ''_p	**1**	0.1298	0.0037	0.7379
Pb	**0.1298**	**1**	0.0534	0.3507
Zn	**0.0037**	**0.0534**	**1**	0.4757
Fe	**0.7379**	**0.3507**	**0.4757**	**1**
	m_2	Pb	Zn	Fe
m_2	**1**	0.0679	0.0399	0.9987
Pb	**0.0679**	**1**	0.0014	0.4872
Zn	**0.0399**	**0.0014**	**1**	0.6048
Fe	**0.9987**	**0.4872**	**0.6048**	**1**

Table A4. Correlation coefficients for the Mž-samples alone.

	σ''_p	Pb	Zn	Fe
σ''_p	**1**	0.9646	0.9772	-0.5332
Pb	**0.9646**	**1**	0.9929	-0.5447
Zn	**0.9772**	**0.9929**	**1**	-0.4972
Fe	**-0.5332**	**-0.5447**	**-0.4972**	**1**
	m_2	Pb	Zn	Fe
m_2	**1**	0.9781	0.9874	-0.5439
Pb	**0.9781**	**1**	0.9929	-0.5447
Zn	**0.9874**	**0.9929**	**1**	-0.4972
Fe	**-0.5439**	**-0.5447**	**-0.4972**	**1**

Table B4. p-values for the Mž-samples alone.

	σ''_p	Pb	Zn	Fe
σ''_p	**1**	4.5e-04	1.5e-04	0.2178
Pb	**4.5e-04**	**1**	8.2e-08	0.2061
Zn	**1.5e-04**	**8.2e-08**	**1**	0.2562
Fe	**0.2178**	**0.2061**	**0.2562**	**1**
	m_2	Pb	Zn	Fe
2	**1**	1.3e-04	3.4e-05	0.2069
Pb	**1.3e-04**	**1**	8.2e-06	0.2061
Zn	**3.4e-05**	**8.2e-06**	**1**	0.2562
Fe	**0.2069**	**0.2061**	**0.2562**	**1**